THE JOURNAL OF PHYSICAL CHEMISTRY C
A JOURNAL OF THE AMERICAN CHEMICAL SOCIETY

pubs.acs.org/JPCC

Article

Hydrogen-Driven Surface Segregation in Pd Alloys from Atomic-Scale Simulations

Pernilla Ekborg-Tanner and Paul Erhart*

Cite This: J. Phys. Chem. C 2021, 125, 17248−17260

Read Online

ACCESS | Metrics & More | Article Recommendations | Supporting Information

ABSTRACT: The safe widespread application of hydrogen-based fuels requires sensors that are long-term stable, inexpensive, hydrogen-specific, and have a short response time. In this regard, optical sensing based on nanostructured Pd alloys has shown great potential, but challenges remain, including understanding and controlling the surface composition under operation conditions. While the latter is crucial for long-term functionality and stability, it is experimentally very challenging to obtain accurate atomic-scale information. Here, we therefore scrutinize the behavior of two particularly relevant surface alloys, {111} AuPd and {111} CuPd, in H environments ranging from vacuum to fully covered surfaces. To this end, we employ a combination of alloy cluster expansions trained using density functional theory calculations, Monte Carlo simulations, and thermodynamic analysis to obtain the H coverage as well as the layer-by-layer composition of the near-surface region as a function of H partial pressure, temperature, and bulk composition. To overcome the symmetry reduction implicit to surface systems, we exploit local symmetries, which enables us to achieve accurate and reliable models at a low computational cost. In the case of AuPd, Au segregates to the surface in vacuum while Pd segregates to the surface at 100% H coverage, and the transition between these regimes occurs over a narrow H pressure interval. In the case of CuPd, on the other hand, the H coverage varies much more gradually with H pressure and is coupled to a nonmonotonic variation of the Cu concentration in the topmost surface layer. While there is a pronounced Cu depletion both at 0 and 100% H coverage, Cu enrichment is observed at 50% coverage at Cu bulk concentrations up to at least 10%, providing a nontrivial explanation for an apparent discrepancy between experiment and calculations that was observed previously. At the same time, layer 2 continuously shifts from Cu enrichment to Cu depletion with increasing H coverage. The results demonstrate the rich behavior that can result from the coupling of metal−metal and metal−hydrogen interactions at surfaces, even in apparently simple but concentrated systems. Moreover, they underline the advantages of simulations that account for temperature and pressure effects as well as models that can accurately capture the interactions over a wide composition range.

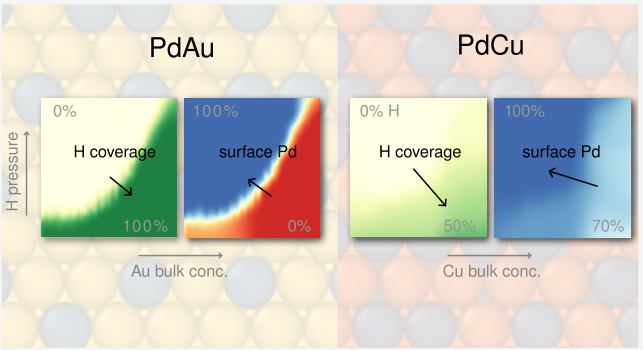

INTRODUCTION

Given the urgent need to replace fossil fuels in the transport sector, hydrogen has emerged as a candidate fuel. Due to the high gravimetric energy density and the possibility to produce hydrogen gas from naturally abundant and green sources,[1] hydrogen fuel cells have recently gained attention in the field of heavy-duty vehicles such as trucks,[2] buses,[3] and trains[4] where weight and material abundance might be an issue for other green technologies such as battery electric vehicles. There are, however, a number of issues related to production,[1,5] storage,[1,6] and safety[7] that need to be solved before hydrogen fuel cell vehicles can be deployed at a large scale. The present work is related to the safety aspect and specifically the need for reliable hydrogen sensors to enable safe handling of potential hydrogen leaks. A promising hydrogen (H) sensor technology is based on the localized surface plasmon resonance (LSPR) response of palladium (Pd) nanoparticles (NPs).[8−11] Essentially, the plasmonic response of a Pd NP red-shifts with hydrogen uptake, which can be monitored to probe the hydrogen content in the environment. There is, however, a need for further optimization of such systems.[12] Pure Pd sensors suffer from hysteresis between the H absorption and desorption half-cycles[13] and carbon monoxide (CO) poisoning.[14] These effects directly limit the reliability and stability of LSPR-based H sensors. Fortunately, a promising solution exists, namely, alloying Pd with other metals: The observed hysteresis is caused by the first-order phase transition between Pd and Pd:H, which can be suppressed by alloying with gold

Received: January 22, 2021
Revised: July 15, 2021
Published: July 28, 2021

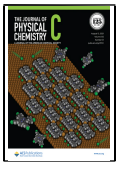

https://doi.org/10.1021/acs.jpcc.1c00575
J. Phys. Chem. C 2021, 125, 17248−17260

(Au),[15] resulting in hysteresis-free sensors.[12−14] CO poisoning is attributed to CO molecules binding to the surface, blocking potential H adsorption sites. The CO binding energy is known to be sensitive to the surface composition,[16−18] and alloying with copper (Cu) has been found to inhibit CO poisoning.[12,14] Recent efforts show that alloying with both Au and Cu can solve both issues simultaneously,[19] bringing forward AuCuPd NPs as a candidate for next-generation H sensors.

The improvements offered by alloying Pd NPs with other metals demonstrate how increasing the degrees of freedom in a system introduces greater tunability. Multicomponent systems are, however, subject to issues related to chemical ordering and/or surface segregation. The surface composition is of utmost importance for the suggested devices, since H_2 uptake/release requires the surface to catalyze H_2 dissociation and also LSPR is intrinsically a surface phenomenon. Understanding the segregation behavior in different atmospheres is thus crucial to obtain sensors that are not only functional but also sustain long-term operation. Surface segregation in binary systems has been studied extensively with experimental and computational methods for the past decades, in particular under vacuum conditions, and it is known that adsorbates can have a substantial impact on the segregation behavior.[17,20−23] Generally, it is found that Au segregates to the surface relative to Pd in vacuum[24−30] and that Pd segregates to the surface relative to Au and Cu in a hydrogen environment.[29] There is less of a consensus regarding CuPd in vacuum, and different segregation behaviors have been suggested.[25,26,29,31−35]

This background provides motivation for the present work, in which we study the surface segregation of Pd alloyed with Au or Cu as a function of H partial pressure, using atomic-scale simulations. We study the entire concentration range for AuPd but limit our study of CuPd to structures with at least 50% Pd, which is sufficient for comparison with the intended experimental work[14,19] and is also indicated by the presence of the body-centered cubic phase in the CuPd phase diagram at 50%.[36] Alloys are challenging to model due to their large configuration spaces. Ideally, one would use ab initio methods such as density functional theory (DFT) to evaluate energies, but it is practically impossible to sample the configuration space using such methods due to the computational expense. There are a few ways to tackle this problem, such as studying a relatively small number of selected configurations using DFT[17,37,38] or using a model Hamiltonian based on some generalized model[24,29,32] or machine learning.[28,39] In this work, we use cluster expansion (CE) models to map out the energy as a function of the atomic configuration, which is a convenient way of bridging the gap between ab initio level accuracy and the computational efficiency needed to sample the vast configuration space. Constructing a CE for surfaces is significantly more challenging compared to bulk due to the large number of symmetrically inequivalent sites. In this work, we present an approach of introducing local symmetries to mitigate this issue and drastically reduce the number of parameters in the CE. Additional challenges arise when introducing adsorbates, which can be handled at different levels of complexity. A rather simple approach is to construct a CE of the system in vacuum to generate configurations of interest and study adsorption on these.[40] Another option is to implicitly introduce adsorbates in the CE by constructing models for a particular adsorbate coverage and set up the training set accordingly. The most general option is to explicitly include the adsorbate sites in the CE which allows for variable coverage.[41,42] This is the approach chosen in the present work, which also allows us to access the chemical potential of H during Monte Carlo (MC) sampling and relate it to the H partial pressure. The connection between partial pressure and surface coverage and/or segregation is often not included in theoretical studies, but is important for accurate comparison to experimental studies. The remainder of this paper is organized as follows. First, we introduce the computational methods used in this work including the CE formalism, DFT calculations, and thermodynamic modeling via MC simulations. Second, we present our results by first assessing the accuracy and reliability of our CE models and then analyzing the obtained H coverage and surface segregation behavior. We provide quantitative predictions for the variation of the surface composition with temperature, partial pressure, and bulk composition. Specifically, we find that for Pd-rich systems at room temperature, the surface is fully H-covered at H partial pressures below 1 mbar. In addition, Pd always segregates to the surface in H-rich environments while Au dominates the surface in vacuum. Finally, we discuss the implications of our results and place them in relation to previous studies.

METHODOLOGY

We use atomic-scale simulations to study surface segregation for the AuPd and CuPd systems from complete vacuum to 100% H coverage. For AuPd, the entire concentration range is covered, while for CuPd, we focus on structures with up to 50% Cu, since the intended applications are typically Pd-rich NPs.[14,19] We model surface slabs in the energetically most favorable {111}-direction[24,43] rather than nanoparticles. This can be motivated by the fact that the systems suggested are typically on the 100 nm-scale[19] where bulk and surface sites are in the majority over edge and corner sites. For the H adsorbates, we only consider the energetically favorable face-centered cubic (FCC) adsorption site,[44] and we do not include H subsurface or bulk sites. We thus define 100% H coverage as one monolayer of H in FCC surface sites which is equal to one H atom per surface metal atom.

Cluster Expansions. In the CE formalism, any function f of the atomic configuration $\boldsymbol{\sigma}$ of a crystalline structure can be expressed as[45]

$$f(\boldsymbol{\sigma}) = \sum_{\boldsymbol{\alpha}} f_{\boldsymbol{\alpha}} \Pi_{\boldsymbol{\alpha}}(\boldsymbol{\sigma}) \tag{1}$$

where the sum is over all atomic clusters $\boldsymbol{\alpha}$, $\Pi_{\boldsymbol{\alpha}}$ are orthogonal basis functions spanning the configuration space,[46] and $f_{\boldsymbol{\alpha}}$ are the energetic contributions from each cluster. A cluster is defined as a set of k lattice sites (singlets, pairs, triplets, etc.) and can be classified by its order k and radius r, which is the average distance between cluster sites and the geometric center of mass of the cluster.

All symmetrically equivalent clusters belong to the same orbit. As a result of symmetry, eq 1 can be reduced to a sum over all orbits, where each orbit is represented by one of its clusters $\boldsymbol{\alpha}$ and the basis functions are averaged over all clusters $\boldsymbol{\alpha}'$ in the orbit

$$f(\boldsymbol{\sigma}) = J_0 + \sum_{\boldsymbol{\alpha}} m_{\boldsymbol{\alpha}} J_{\boldsymbol{\alpha}} \langle \Pi_{\boldsymbol{\alpha}'}(\boldsymbol{\sigma}) \rangle \tag{2}$$

Here, $m_{\boldsymbol{\alpha}}$ is the multiplicity of clusters in the orbit represented by $\boldsymbol{\alpha}$ and the effective cluster interactions (ECIs) $J_{\boldsymbol{\alpha}}$ have been

https://doi.org/10.1021/acs.jpcc.1c00575
J. Phys. Chem. C 2021, 125, 17248−17260

introduced. In the present work, the ICET package[47] has been used to construct CEs.

In practice, the summation in eq 2 has to be truncated both with respect to expansion order and cluster size, commonly using cutoff radii. In this work, pairs and triplets are included up to cutoffs of $2.0a_0$ and $1.25a_0$, respectively, where a_0 is the lattice parameter. This choice was made after careful analysis of a large range of cutoffs and results in models with high accuracy and predictive power (Figure S10). To avoid overfitting, we further tune the hyperparameters of the regression algorithm to minimize the Bayesian information criterion (BIC) score which reduced the number of parameters by half. A detailed description of the training procedure can be found in Note S1, Supporting Information.

Since the objective is to study surface segregation, CEs are constructed for 10-layer FCC surface slabs with {111} surfaces and FCC adsorption sites. The CEs are constructed with two sublattices: one for the alloy, which can be occupied by the metal atoms (Au and Pd or Cu and Pd), and one for adsorption site, which can be occupied by a H atom or a vacancy.

Introducing Local Symmetries. In surface slabs, each atomic layer represents a symmetrically inequivalent atomic site, in contrast to bulk FCC structures where there is only one inequivalent site. This means that the number of orbits quickly grows with the number of layers, since for example nearest neighbor (NN) pairs between sites A−A and sites A−B are symmetrically distinct. One approach to mitigate this issue is to only include certain regions in the CE, for example only the near-surface region,[48] and keep the remainder of the material in a fixed configuration. If the orbits in question are far from the surface, however, interactions are expected to converge to the interactions in a bulk material where for example all NN pairs are equal. This understanding can be used to substantially reduce the complexity of a CE model and the number of distinct ECIs.

One possibility is to implement this prior knowledge of the system under study via a Bayesian approach, imposing correlations between ECIs via suitable priors.[49] In the present work, we employ a more direct approach, exploiting local symmetries to merge similar orbits based on the following principles (Figure 1)

1. Define which sites are to be considered as bulk sites
   - Singlets: sites in layer 4 and inward
   - Pairs: sites in layer 3 and inward
   - Triplets: sites in layer 2 and inward
2. Identify all orbits with the same order and radius
3. Merge orbits with at least one bulk site

The number of bulk sites increases with orbit order to obtain a smooth transition from surface to bulk. This approach, which has been implemented in the ICET package, allows us to drastically reduce the number of ECIs. For instance, the number of ECIs is reduced from 267 to 97 for a binary 10-layer slab with the selected cutoffs. As a result, the number of reference calculations can be greatly reduced, the construction of CEs is simplified and their sampling sped up.

We have found that this simple approach results in models that are less prone to overfitting, produce accurate segregation energy predictions, and maintain low cross-validated (CV)-root mean square errors (RMSEs) (Figure S9). As an added benefit, structures with any number of layers can be included in training and similarly the resulting CE can be applied to

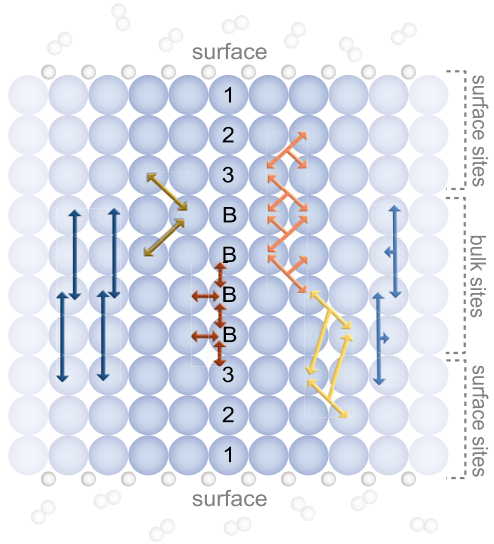

Figure 1. Schematic illustration of the merging of orbits of a crystalline surface slab with 10 layers and periodic boundary conditions in the surface plane. For the alloy lattice, there are three distinct surface singlets (1−3) and one bulk singlet (B), as indicated by the numbers. The arrows are examples of pair and triplet orbits that are merged, with each color representing one orbit. Note that merged pairs can include sites in layer 3 and merged triplets can include sites in layers 2 and 3. Adsorption sites are not affected by the merging.

structures with any number of layers. One can also imagine future extensions where the training data consists of a mix of bulk, surface, and possibly even nanoparticle structures to build multidimensional CEs.

Training Data Generation. Training data sets consisting of mixing energies for different atomic configurations are needed for training CEs. In this work, total energies E^{tot} are obtained using DFT calculations (see Computational Details) and converted into mixing energies E^{mix} according to

$$E^{\mathrm{mix}} = \frac{E^{\mathrm{tot}} - n_{\mathrm{Pd}}E^{\mathrm{tot}}_{\mathrm{Pd}} - n_{\mathrm{M}}E^{\mathrm{tot}}_{\mathrm{M}} - n_{\mathrm{H}}E^{\mathrm{tot}}_{\mathrm{H}}}{n_{\mathrm{Pd}} + n_{\mathrm{M}}} \quad (3)$$

where M = Au or Cu, n_X is the number of atoms of species X, E^{tot}_X is the total DFT energy per atom obtained from a 10-layer slab in vacuum for the metals and for H, and $E^{\mathrm{tot}}_{\mathrm{H}}$ is the difference in energy for a 10-layer Pd slab with and without a H atom adsorbed.

The predictive ability of a CE is sensitive to the selection of atomic configurations included in the training set, and predictions for configurations that are not well represented by the training set will generally be less reliable. For the most part, we have chosen an approach where structures are generated iteratively by constructing a cluster vector (with elements $m_{\alpha}\langle\Pi_{\alpha}'(\boldsymbol{\sigma})\rangle$ from eq 2) orthogonal to prior cluster vectors, similar to the approach in ref 50. The space of cluster vectors, however, cannot be completely orthogonal due to correlations between orbits. In addition, we impose the following constraints on the cell dimension and concentration. The cell dimension is randomly selected (with uniform distribution) from the set of supercells with up to three atoms in each direction parallel to the surface. The alloy concentration is randomly selected from a triangular distribution with maximum at 50%. The orthogonal cluster vector is then matched to the closest structure satisfying the

https://doi.org/10.1021/acs.jpcc.1c00575
J. Phys. Chem. C 2021, 125, 17248−17260

constraints, using ICET functionality. This process was carried out for 0% H coverage, 100% H coverage, and variable H coverage separately, resulting in an overrepresentation of the first two categories.

In addition to this approach, we included data sets consisting of random configurations as well as low-energy structures found by simulated annealing (SA) using intermediate CE models (Thermodynamic Modeling). Furthermore, we included configurations used for calculating segregation energies in the dilute limit and adsorption energies (Model Construction). This procedure was established by extensive testing as well as trial and error. A detailed description of the data sets used is provided in Table S1.

Computational Details. Reference DFT calculations were carried out using the projector augmented method[51,52] as implemented in VASP.[53,54] The van der Waals density functional method[55,56] with consistent exchange,[57] which has been shown to be very well suited for transition metals,[58] was employed to represent the exchange-correlation potential. The atomic positions were relaxed until residual forces were less than 10 meV/Å. The cell metric was kept fixed at a lattice parameter obtained by interpolating results from previous DFT calculations of bulk systems, where both the atomic positions and the cell metric were relaxed, using the same computational parameters. A vacuum region of 20 Å was introduced along the direction of the surface normal to minimize interactions between periodic images. For all calculations, the plane-wave cutoff energy was set to 400 eV. During relaxations the Brillouin zone was sampled with a $\boldsymbol{k}$-point density of 0.2 Å^{-1} and first-order Methfessel−Paxton smearing with a width of 0.1 eV. Final energy calculations were carried out for the relaxed structures with a $\boldsymbol{k}$-point density of 0.1 Å^{-1} and the tetrahedron method with Blöchl corrections using a smearing width of 0.05 eV.

Thermodynamic Modeling. In the present work, the CE models were sampled via MC simulations using the MCHAMMER package[47] for two purposes. First, to extend the training data set by carrying out SA where the temperature was lowered exponentially from 800 to 100 K and the final configuration was added to the training set. Second, isothermal simulations were carried out to obtain average configurations at various temperatures, H chemical potentials, and alloy concentrations to study surface segregation and H coverage. The MC simulation was run in the canonical or semi-grand canonical (SGC) ensemble. In the canonical ensemble, each trial step consists of interchanging the species of two sites[59] such that the total concentration remains constant. The change in the thermodynamic potential, which enters the Metropolis criterion, is then $\Delta\Phi = \Delta E^{\mathrm{mix}}$. In the SGC ensemble, the chemical potential difference $\Delta\mu$ between the allowed species at a specific site is controlled, and each trial step consists of swapping the occupancy at one site.[60] The change in thermodynamic potential is then $\Delta\Phi = \Delta E^{\mathrm{mix}} \pm \Delta\mu$. The MCHAMMER package handles CEs with multiple sublattices by, in each trial step, randomly selecting one of the sublattices (with equal probability in the present work) and executing a trial step. This approach corresponds to a system in full equilibrium, where the alloy has time to rearrange its atomic configuration upon a change in H pressure. For the segregation studies at a certain H coverage, we used the canonical ensemble for the entire system. For the studies of H coverage and segregation, we used the canonical ensemble for the alloy lattice and the SGC ensemble for the H lattice, which gives us access to the H chemical potential and, in extension, the H partial pressure. We thus treat the metal sublattice as a closed system (appropriate given the kinetics of this system). The adsorbate lattice, on the other hand, is handled as an open system, which accounts for the fact that the adsorbate can readily exchange H atoms with the H_2 reservoir in the atmosphere.[15]

Chemical Potential to Partial Pressure Conversion. To convert the H chemical potential to partial pressure, we rely on previous work by Rahm et al.[15] on the bulk Pd:H system. The H chemical potential $\mu_{H_2}(T, p_{H_2})$ is related to the H partial pressure p_{H_2} via

$$\mu_{H_2}(T, p_{H_2}) = \mu^{\circ}_{H_2}(T) + k_B T \ln \frac{p_{H_2}}{p^{\circ}_{H_2}} \tag{4}$$

where $\mu^{\circ}_{H_2}(T)$ is the temperature-dependent chemical potential of H_2 at a reference pressure $p^{\circ}_{H_2}$. In ref 15, $\mu^{\circ}_{H_2}(T)$ is determined by fitting the observed chemical potential at the phase transition between Pd and Pd:H to the experimentally measured partial pressure at the phase transition, which results in the following relation

$$p_{H_2} = \exp\left(\frac{2\mu_H + \Delta P(T)}{k_B T}\right)$$

where $\mu_H = (1/2)\mu_{H_2}$ is the chemical potential of adsorbed H and $\Delta P(T)$ is a result of the fit. It should be noted that this conversion is based on the ideal gas assumption, which fails at very high pressures.[15]

To apply this conversion to our problem, we need to correct for the differences in mixing energy definition. The chemical potential is derived from the free energy

$$\mu_H = \frac{\partial F}{\partial n_H} = \frac{\partial (E^{\mathrm{tot}} - TS)}{\partial n_H}$$

The relation between the total energy E^{tot} and the CE mixing energy E^{mix} is given by eq 3, where the metal terms disappear due to the derivative with respect to n_H. We find that the correction for μ_H is the difference between the H contribution in the mixing energy calculation, E^{tot}_H in eq 3, and define

$$E_{\mathrm{corr}} = E^{\mathrm{tot}}_{\mathrm{H,slab}} - E^{\mathrm{tot}}_{\mathrm{H,bulk}} = -0.4042 \text{ eV}$$

Finally, we obtain the conversion relation between H chemical potential and partial pressure

$$p_{H_2} = \exp\left(\frac{2\tilde{\mu}_H + 2E_{\mathrm{corr}} + \Delta P(T)}{k_B T}\right) \tag{5}$$

where $\tilde{\mu}_H$ is the H chemical potential specified during MC simulations of our CEs in the SGC ensemble. We note that the chemical potential to pressure conversion is sensitive to small changes of parameters,[15] as a result of which the pressure values presented below need to be considered as estimates.

RESULTS

Model Construction. CEs were constructed for the AuPd:H and CuPd:H systems with FCC adsorption sites. The models yield CV-RMSEs of 2.6 and 2.7 meV/atom, respectively, which is small compared to the energy interval studied (Table 1 and Figure S4). The models display very good agreement with the reference data over the entire range

https://doi.org/10.1021/acs.jpcc.1c00575
J. Phys. Chem. C 2021, 125, 17248−17260

Table 1. CV-RMSE, Coefficient of Determination (R^2), Number of Structures in the Training Set, and Number of Features of the CEs

system	CV-RMSE (meV/atom)	R^2	number of structures	number of features
AuPd:H	2.6	1.00	651	35
CuPd:H	2.7	0.99	283	39

of concentrations studied for both AuPd:H (Figure 2a) and CuPd:H (Figure 2b) as well as with adsorption energy

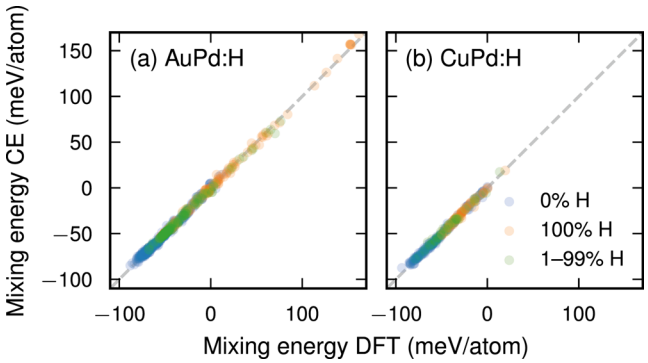

Figure 2. Comparison of mixing energies as calculated by DFT and as predicted by CEs for all structures in the training set for AuPd:H (a) and CuPd:H (b). The structures are colored according to their H coverage. The CE predictions agree well with the DFT calculations regardless of H coverage.

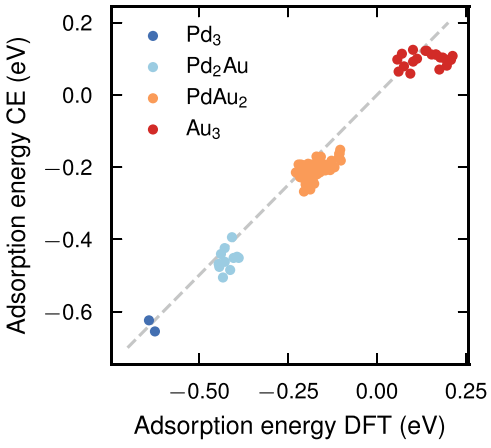

Figure 3. Comparison of adsorption energies as calculated by DFT and as predicted by the AuPd:H CE for five Pd_{75}/Au_{25} configurations (see also Figure S3). The color indicates the chemical composition of the three atoms below the H site. The CE predictions agree well with the DFT calculations.

calculations for selected configurations (Figure 3). Regression hyperparameters were tuned to minimize BIC, which reduced the number of features from 98 to 35 and 39, respectively. The ECIs decrease with cluster radius for the final models (Figure S6), indicating that the cutoffs are sufficiently large.

To further assess the models, we consider segregation energies, which were calculated for 2 × 2 × 10 slabs consisting of one type A atom and a majority of type B atoms by moving the A atom between the layers. The segregation energy for A in B at layer x is then the energy difference induced by moving the A atom from the middle of the slab to layer x

$$E_x^{\text{seg}} = n(E_{\text{A in } x}^{\text{mix}} - E_{\text{A in bulk}}^{\text{mix}})$$

where n is the number of atoms (excluding H), $E_{\text{A in } x}^{\text{mix}}$ is the mixing energy when A is in layer x and $E_{\text{A in bulk}}^{\text{mix}}$ is the mixing energy when A is in the middle of the slab, with mixing energies as defined in eq 3.

The segregation energies from the CEs are in good agreement with the DFT calculations (Figure 4). The case of

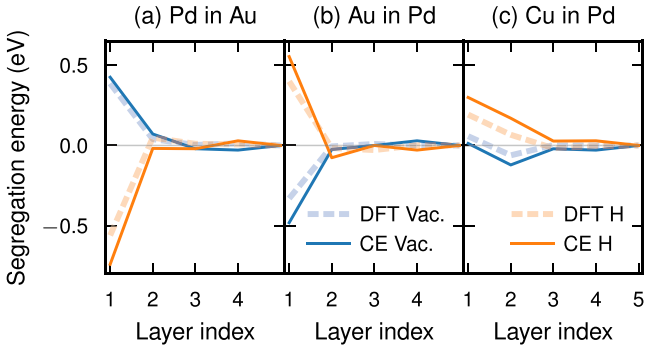

Figure 4. Segregation energies for (a, b) AuPd and (c) CuPd in the dilute limit in vacuum (blue) and at 100% H coverage (orange) from DFT and CE calculations. The segregation energies from CEs are in good agreement with the DFT calculations.

one Pd in Cu is excluded since the training set for CuPd:H only includes structures with at least 50% Pd. Segregation energies provide information about the segregation behavior in the dilute limit. The results suggest for the AuPd system to display surface depletion of Pd in vacuum and enrichment in the presence of adsorbed H (Figure 4a,b). For the CuPd system in vacuum, we expect a slight depletion of Cu at the surface, followed by an enrichment in the second layer (Figure 4c). In the presence of adsorbed H, we expect depletion of Cu at the surface and subsurface.

Environment Dependence of Segregation and Adsorption. While the segregation energies in the dilute limits indicate segregation preferences in vacuum and H-rich environments, in practice one is commonly interested in compositions in the percent range in an environment characterized by H partial pressure and temperature. Here, we access this concentrated region at variable H chemical potential using MC simulations in the canonical (alloy sublattice) and SGC (H sublattice) ensembles based on CE models, which also enables us to handle the effect of temperature. As outlined in the Chemical Potential to Partial Pressure Conversion section, the H chemical potential can be converted to H partial pressure, which allows us to study the H coverage and layer-by-layer composition of AuPd and CuPd alloys as a function of H partial pressure and temperature.

We begin with the simpler case of H coverage on pure Pd by studying the average site occupancy of the adsorbate sites obtained during MC simulations at varying H chemical potential. We then continue with the alloy systems based on MC simulations at varying chemical potentials of both H and the alloying element where the average site occupancy of the adsorbate as well as each layer of the surface slab is recorded. We define layers 4 and 5 as the bulk region and the bulk concentration is defined as the average over this region. Layers

https://doi.org/10.1021/acs.jpcc.1c00575
J. Phys. Chem. C 2021, 125, 17248−17260

1−3 are defined as the near-surface region and each layer is studied independently, focusing on the surface (layer 1) and subsurface (layer 2). The behavior of layer 3 is commonly almost identical to the bulk and therefore not discussed in further detail.

H on Pure Pd. In contrast to Cu and Au, adsorption of H on Pd is energetically rather favorable (Figure S2) meaning that we expect H adsorption on Pd to occur at low pressures (compared to ambient conditions). Here, we present results from MC simulations of pure Pd at varying H chemical potential based on the AuPd:H CE. Note that predictions for Pd:H agree between the AuPd:H and CuPd:H CEs (Figure S5). Our simulations show that the H coverage on Pd changes from 0 to 100% over a chemical potential interval of about 0.5 eV at 300 K, which widens slightly with increasing temperature (Figure 5a). At 300 K, this corresponds to full coverage already

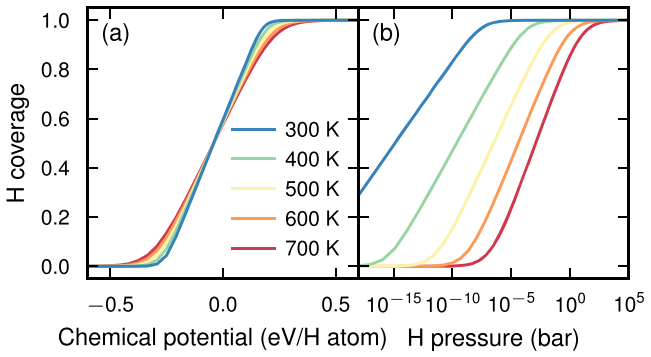

Figure 5. H coverage (adsorption isotherms) over pure Pd as a function of (a) H chemical potential and (b) H partial pressure at different temperatures. At 300 K, the surface is fully covered already around 10^{-7} bar, while at higher temperatures, the coverage varies over the pressure range typically relevant for experiments. The shift from (a) to (b) is the direct result of eq 4.

at 10^{-7} bar H partial pressure (Figure 5b). Increasing the temperature pushes the transition in H coverage to higher pressures. As a result, we find that at 600 K the H coverage varies in the mbar to bar range, which is common in experiments.

H−Au Interplay. When Pd is alloyed with Au, the H coverage varies over a much narrower H chemical potential interval than in the case of pure Pd (Figure 6a), exhibiting a step-like behavior. This is reasonable considering the facts that the AuPd system favors strong segregation of Au to the surface in vacuum and that H adsorption is unfavorable on Au (Figures 3 and S2). Even at very low Au bulk concentrations, Au atoms at the surface are able to block H from the surface up to considerably higher H chemical potentials compared to Pd. As a result, the H coverage switch is highly correlated with the Au surface concentration (Figure 6b). In the regions corresponding to 0 or 100% H coverage, the surface composition varies only gradually with bulk composition (as discussed in more detail in the Surface Segregation at Specific H Coverages section).

Upon conversion of the H chemical potential to H partial pressure, one observes that the transitions in H coverage (Figure 7a−d) and surface composition (Figure 7e−h) occur over a relatively narrow pressure range (see also Figure 8a) compared to pure Pd and the H partial pressure at which the transition occurs, varies with Au bulk concentration and temperature over several orders of magnitude. In the Pd-rich

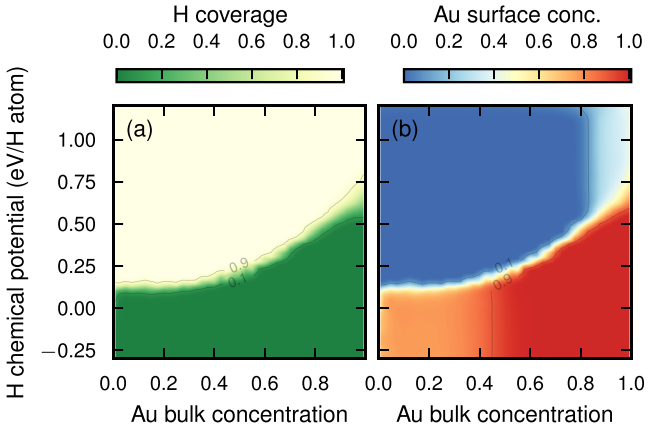

Figure 6. (a) H coverage and (b) Au surface content as a function of H chemical potential and Au bulk concentration at 300 K obtained by MC simulation. The H coverage switches from 0 to 100% over a very narrow chemical potential interval, which shifts upward with increasing Au content. Simultaneously, the surface composition switches from Au-dominant to Pd-dominant.

end, the transition occurs at very low pressure for low temperatures and at 300 K, the surface is completely covered at 10^{-9} bar. At higher temperatures, higher pressures are required to fully cover the surface and at 600 K the corresponding value is approximately 10^{-1} bar.

In Figure 7, we also show the pressure at which the concentration of H is expected to reach 1 and 5%, respectively, based on previous work on the AuPd:H bulk system.[15] Our models do not take into account H absorption to the subsurface and bulk of the alloy and as a consequence, they are not valid for pressures at and above which H sorption into the bulk occurs. The bulk absorption lines thus indicate an approximate validity limit of our models. Crucially, though since this limit is always firmly above the region in which the transition in H coverage and surface composition takes place. Specifically, we observe that for AuPd, the surface is always fully H-covered (Figure 7a−d) and predominantly composed of Pd before the H uptake exceeds 1% (Figure 7e−h).

H−Cu Interplay. When Pd is alloyed with Cu, the H coverage varies over a relatively wide H chemical potential interval similar to pure Pd (Figure 9a). This is qualitatively expected considering that the Cu surface concentration is rather low throughout the studied configuration space such that alloying should have a less significant impact on H coverage (compared to AuPd), and in addition, H adsorption on Cu is favorable (Figure S2, in contrast to Au).

We observe nontrivial correlations between H partial pressure and bulk composition in the first and second alloy layers (Figure 9b,c). Counterintuitively, it appears as if adsorption to the surface has a greater impact on the subsurface layer than the surface. Up to 30% Cu bulk concentration, we can distinguish three regions. First, at 0% H coverage (essentially in vacuum), there is no Cu at the surface but a pronounced Cu enrichment in layer 2. Then, at about 50% H coverage, we have a significant amount of Cu at the surface (even a slight excess in the dilute Cu limit) and a less pronounced Cu enrichment in layer 2. Finally, at 100% H coverage, there is essentially no Cu in either surface or subsurface. Above 30% Cu bulk concentration, we observe similar but slightly shifted trends.

https://doi.org/10.1021/acs.jpcc.1c00575
J. Phys. Chem. C 2021, 125, 17248−17260

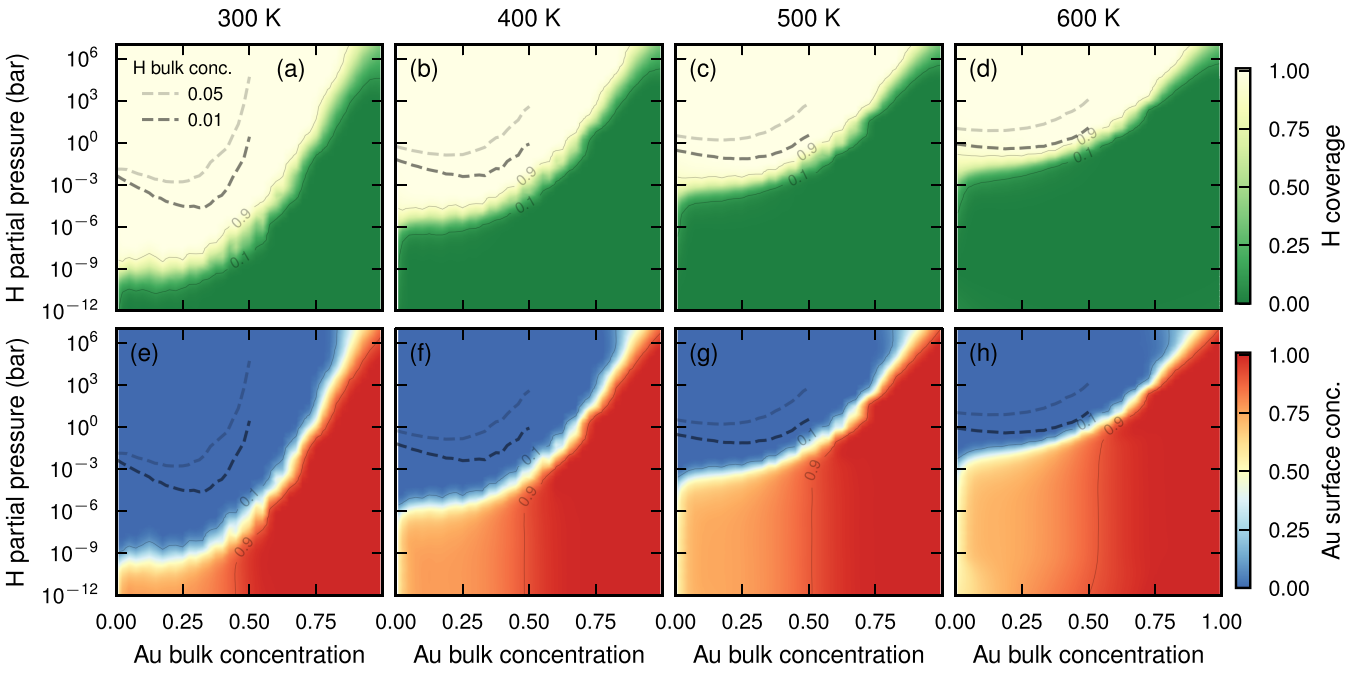

Figure 7. (a–d) H coverage and (e–h) Au surface content as a function of H partial pressure and Au bulk concentration at different temperatures (as indicated by the column labels) obtained by MC simulation. The dashed lines show the pressure at which the H bulk concentration reaches 1 and 5%, respectively, according to ref 15. They thus indicate the approximate upper validity limit of our models, which do not include H in subsurface or bulk sites.

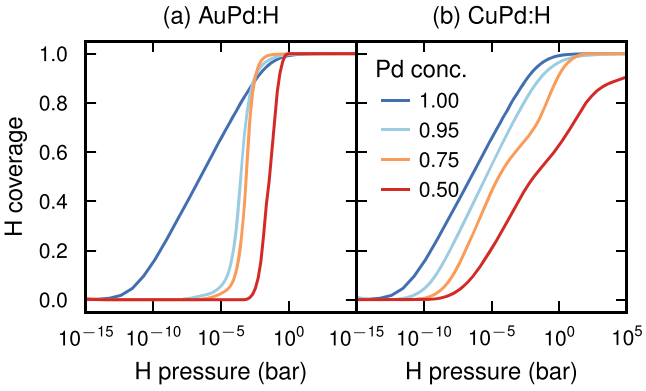

Figure 8. H coverage as a function of H partial pressure at 500 K for several bulk concentrations of (a) Au and (b) Cu. The adsorption isotherms are significantly steeper for AuPd compared to pure Pd and CuPd.

After converting the H chemical potential to pressure, we find that in the Pd-rich end, the surface is mostly H-covered already at 10^{-6} bar at room temperature (Figure 10a). The H coverage varies over a wide pressure range, similarly to pure Pd (Figure 8b). The pressure needed for full coverage increases with Cu content and temperature, and at 600 K has risen to approximately 1 bar (Figure 10a–d). The dashed lines in Figure 10 indicate 1 and 5% H uptake in the bulk Pd.[15] Similarly to the case of AuPd (Figure 7), they are included here to indicate the threshold above which the subsurface and bulk sites are being occupied and hence the limit of the application range of the CEs developed here. We do not have access to a corresponding CE for CuPd:H in bulk and therefore the respective pressures are only indicated in the pure Pd limit. Since it is, however, experimentally known that the hydrogenation pressure increases with Cu content,[14] one can expect the actual pressures to curve upward toward higher values with increasing Cu content.

Even at the lowest H pressures considered here (10^{-12} bar) the H coverage is nonzero at 300 K (Figure 10a,e,i). At the same time, there is a slight Cu enrichment at the surface, which becomes maximal at around 50% H coverage (see also the Surface Segregation at Specific H Coverages section). In contrast, there is a Cu depletion both under vacuum conditions (leading to 0% H coverage) and at higher H pressures (leading to 100% coverage).

The unusual nonmonotonic variation of the surface composition with partial pressure and its correlation with H coverage are also present at higher temperatures (Figure 10f–h,j–l). With increasing temperature the pressure that yields a 50% H coverage and a maximum in the Cu excess shifts up, leading to a nose-like feature in surface composition maps (Figure 10e–h).

At all temperatures, the composition of the topmost surface layer is to some extent correlated with layer 2 (Figure 10j–l), for which one observes at low H pressures a Cu enrichment relative to the bulk that turns into a Cu depletion at high pressures. This behavior is described in more detail in the next section.

Surface Segregation at Specific H Coverages. Given the results presented in the two previous sections, it is indicated to study the surface segregation at specific H coverage more closely. This also provides a more direct link to earlier studies that considered the behavior in the dilute limits of 0 and 100% coverage. For AuPd:H, we only consider 0 and 100% H coverage since the transition occurs over a narrow pressure interval. For CuPd:H, we also consider 50% H coverage, since the transition takes place over a wide pressure interval, exhibiting a nonmonotonic segregation behavior with respect to H coverage (Figures 9 and 10). We present the segregation in terms of layer concentration in the near-surface

https://doi.org/10.1021/acs.jpcc.1c00575
J. Phys. Chem. C 2021, 125, 17248–17260

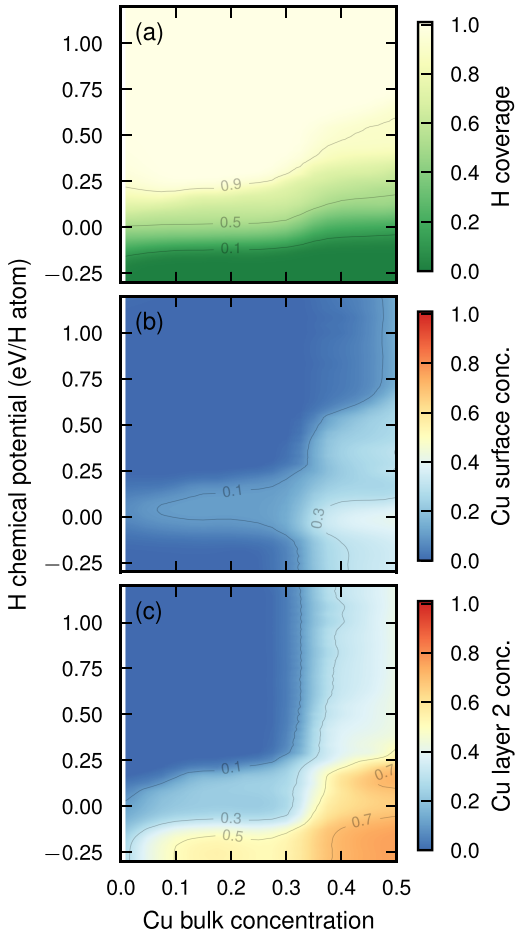

Figure 9. (a) H coverage, (b) Cu surface concentration, and (c) Cu subsurface concentration as a function of H chemical potential and Cu bulk concentration. The composition of the first and second alloy layers is intricately correlated to the H coverage. The latter changes over a relatively wide chemical potential interval, which is weakly dependent on the Cu bulk concentration.

region (layers 1−3) as a function of bulk concentration (layers 4 and 5).

For the AuPd system at 0% coverage, we observe a very strong enrichment of Au at the surface (Figure 11a). At 300 K, Pd does not enter the surface until the bulk Pd concentration is above approximately 50% and at increased Pd content, the surface Pd concentration plateaus at approximately 25%. In the second layer, there is a slight Pd excess in the middle of the concentration range (Figure 11c) followed by a slight depletion in the third layer (Figure 11e). This oscillatory behavior is a recurring feature found throughout our studies. In the dilute Au limit, however, the Pd depletion extends throughout the near-surface region.

At 100% H coverage, AuPd displays the opposite segregation behavior with a strong enrichment of Pd at the surface (Figure 11b) and Au does not enter the surface until approximately 75% Au bulk concentration. There is a plateau at 33% Au indicating the presence of an ordered surface phase. In the second layer, we observe a depletion of Pd in both dilute limits, inducing an oscillating concentration profile (Figure 11d). In the intermediate composition range, however, the segregation does not extend to layer 2 and the concentration is comparable to the bulk. The layer 3 composition deviates only slightly from the bulk throughout the concentration range considered here (Figure 11f).

For the CuPd system at 300 K (Figure 12), the segregation profiles generally have more step-like features compared to AuPd (Figure 11), indicating a tendency to order as the system strives to remain at specific surface concentrations. Here, we do not scrutinize these ordering patterns more closely but focus on the general thermodynamic behavior.

At 0% H coverage, we observe Pd enrichment in the topmost surface layer (Figure 12a) followed by a pronounced Cu enrichment in layer 2 (Figure 12d) and a slight Pd excess in layer 3 (Figure 12g). The composition thus oscillates between layers 1−3, as suggested by the CuPd segregation energies in the dilute limit (Figure 4c).

At 50% H coverage, the amount of Cu at the surface increases notably compared to the 0% H coverage limit and there is even a slight Cu excess in the Pd-rich limit at 300 K (Figure 12b). The segregation in layer 2 (Figure 12e) is significantly less extreme compared to the 0 and 100% H coverage cases (Figure 12d,f), with almost no segregation at higher temperatures and a plateau at approximately 25% Cu at 300 K. The concentration in layer 3 is close to the bulk concentration with a weak ordering tendency at 300 K (Figure 12h).

Finally, at 100% H coverage, the CuPd system presents a strong Pd enrichment in the topmost surface layer (Figure 12c) followed by a slightly weaker Pd excess in layer 2 (Figure 12f), in contrast to the otherwise common oscillatory trend. There are no strong segregation tendencies in the third layer (Figure 12i).

Generally, higher temperatures lead to less extreme segregation behavior. At lower temperatures, on the other hand, we observe ordering tendencies in several systems, which lead to step-like features in the variation of the layer concentration with bulk composition (see, e.g., Figure 12a,b,d,e). The strength of the ordering is a result of the competition between energy (which favors ordering) and entropy (which favors disordering).

DISCUSSION

The variation of surface composition with environmental conditions is crucial for the functionality of materials in, e.g., sensing, catalysis, and energy conversion. Accordingly, there has been a sizable number of studies, both experimental and computational, that aim to provide much needed insight into this coupling, in particular with respect to the role of hydrogen. As a result of the size of the parameter space, which includes, e.g., temperature, gas pressure, and bulk composition, as well as limitations of both experimental and computational approaches, the interplay of these factors remains, however, incompletely understood. Experimentally, it is for example difficult to resolve the composition of the surface with layer-by-layer resolution under reactive conditions and for a larger number of samples. On the computational side, limitations include the availability of models that can truthfully represent the interactions between the alloy components as well as the interactions involving hydrogen over a wide range of alloy compositions and H pressures. Here, to overcome these challenges, we therefore combined atomistic MC simulations, CE models that accurately reproduce DFT data as well as thermodynamic analyses to provide a comprehensive description of the surface composition of AuPd and CuPd alloys. This

https://doi.org/10.1021/acs.jpcc.1c00575
J. Phys. Chem. C 2021, 125, 17248−17260

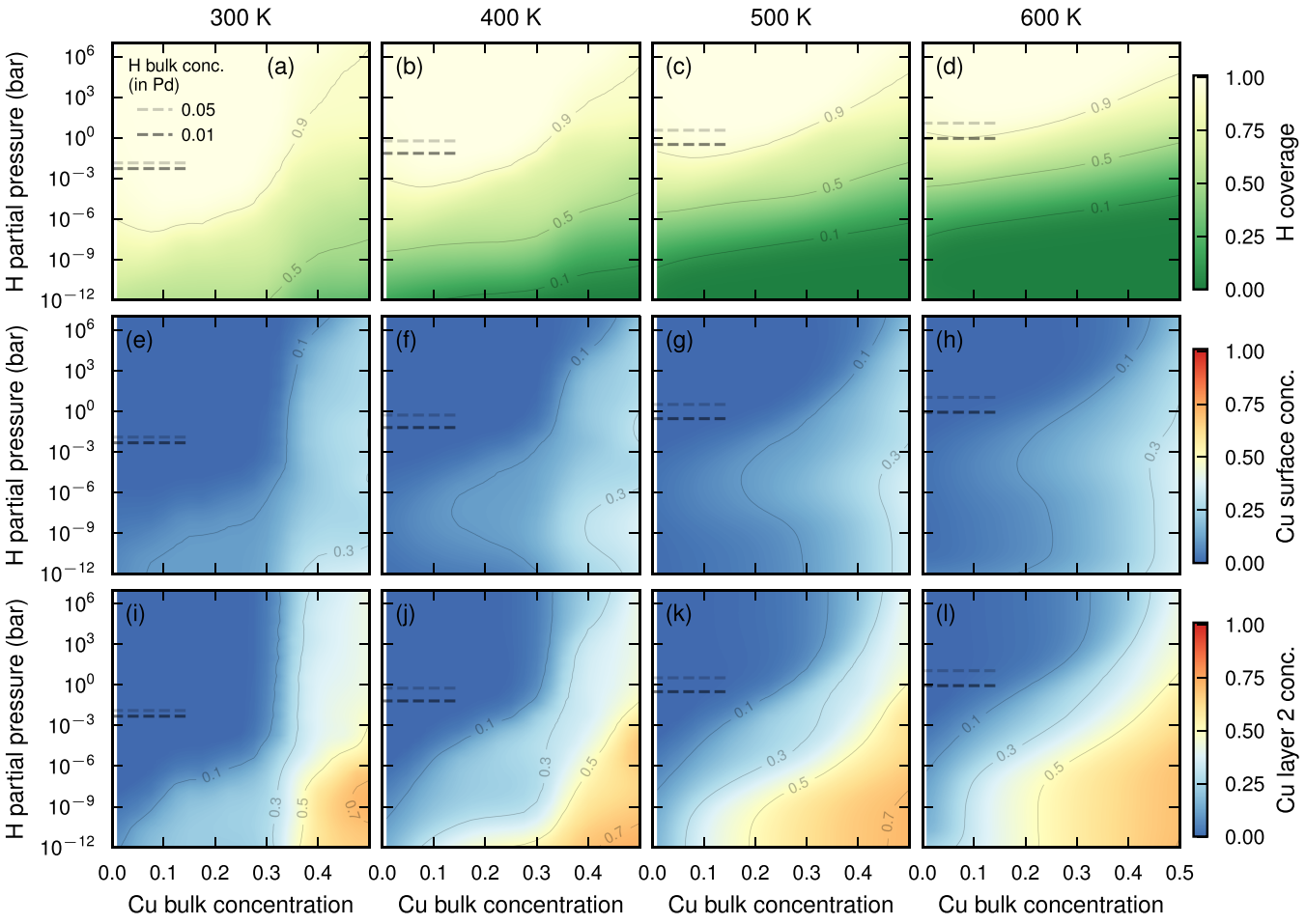

Figure 10. (a–d) H coverage, (e–h) Cu surface concentration, and (i–l) Cu subsurface concentration as a function of H partial pressure and Cu bulk concentration at various temperatures (as indicated by the column labels) obtained by MC simulation. The dashed lines show the pressure at which the H bulk concentration reaches 1 and 5% in pure Pd, respectively; see ref 15. Note that the hydrogenation pressure increases with Cu content[14] which means that the dashed lines should curve upward if we had access to the corresponding CE representation of bulk CuPd:H.

allowed us to reveal the coupling between partial pressure, H coverage as well as surface and bulk composition.

Our analysis shows that the H coverage on pure Pd changes gradually over a rather wide range of pressures (Figure 5b). Since it is experimentally difficult to access this information, measurements are approximate and limited to very low temperatures and pressures.[61] Previous studies assumed, for example, that Pd is fully H-covered at 1 bar with a weak temperature dependence at least up to approximately 500 K.[62] This is fully consistent with our results (Figure 5b), which moreover suggest that at this pressure the H coverage remains above 80% even up to 700 K. Our results are also consistent with observations that at a very low pressure (approximately 10^{-9} bar), Pd is fully H-covered at an extremely low temperature (37 K),[61] partly covered at 300 K,[63] and almost completely free of adsorbed H at 600 K.[63] It should nonetheless be noted that the conversion from chemical potential to pressure via eq 5 is sensitive to changes in the fitted parameters, which needs to be kept in mind when comparing our calculations with experiment.

In contrast to pure Pd, in AuPd alloys, the H coverage changes from 0 to 100% over a very narrow pressure range already for very small Au bulk concentrations (Figure 8). This behavior is coupled to pronounced differences in segregation behavior between 0 and 100% H coverage. While in the absence of H adsorbates (lower H pressure) Au readily segregates to the surface, exactly the opposite behavior is observed in the presence of H adsorbates (higher H pressure), which is in good agreement with previous experimental and theoretical work.[24−30] Hydrogen can thus be thought of as inducing a miscibility gap for the topmost surface layer, even though the AuPd system is fully miscible in the bulk down to ambient temperatures. The pressure at which the transition occurs shifts upward with increasing temperature, which is a direct result of the relation between H chemical potential and H pressure expressed by eq 4. Furthermore, the transition pressure is weakly dependent on Au concentration up to about 40% Au beyond which it rises sharply with composition (Figure 7). The latter composition dependence is reminiscent of the variation of the dielectric function in this alloy system, which can be traced to the gradual filling of the d-band with increasing Au content and the resulting shift of the Fermi energy.[64] This underlying mechanism is likely to also play a role in the present case.

The general trends in the above-described behavior are already evident from the segregation energies in the dilute limit (Figure 4a,b). Partly as a consequence, segregation behavior and H coverage for the {111} AuPd surfaces can be predicted semiquantitatively using a rather simple thermodynamic model based on such information that uses bulk composition and H

https://doi.org/10.1021/acs.jpcc.1c00575
J. Phys. Chem. C 2021, 125, 17248−17260

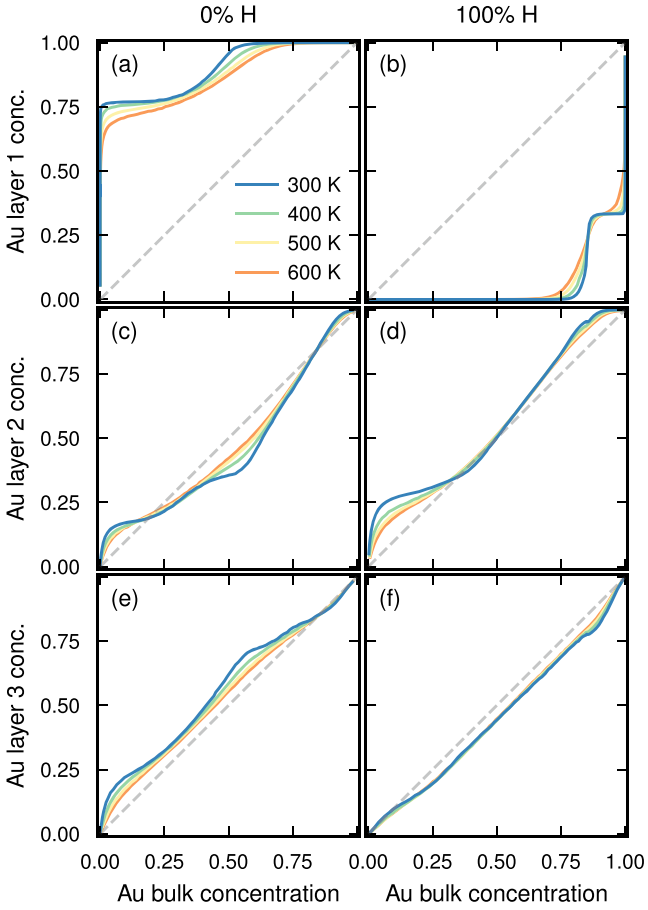

Figure 11. Layer-by-layer concentration in the near-surface region of AuPd as a function of the bulk concentration at 0% (left column) and 100% (right column) H coverage. The first row (a, b) displays the concentration of the topmost surface layer, the second row (c, d) layer 2, and the third row (e, f) layer 3. One observes pronounced segregation of Au to the surface in (a) the absence of H and of Pd in (b) the presence of H. The extent of the segregation diminishes quickly away from the surface and generally follows an oscillatory pattern with an excess being followed by a depletion in the next layer.

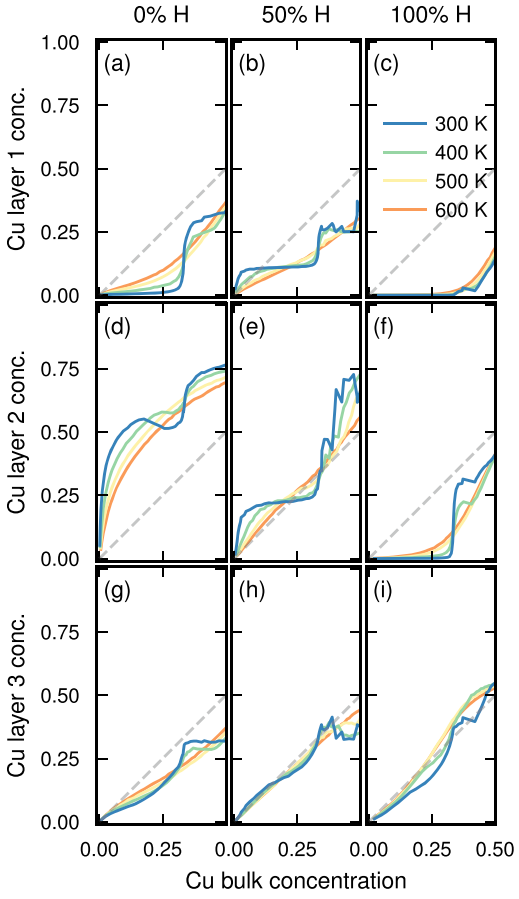

Figure 12. Layer-by-layer concentration in the near-surface region of CuPd compared to bulk at 0% (left column), 50% (middle column), and 100% (right column) H coverage. The first row (a–c) displays the concentration of the topmost surface layer, the second row (d–f) layer 2, and the third row (g–i) layer 3. Pd generally segregates to the surface, but the tendency does not vary monotonously with H coverage. Layer 2 also displays pronounced segregation tendencies, with a strong Cu excess in vacuum and a strong Pd excess at 100% H coverage. The oscillatory pattern between the layers (observed for AuPd in Figure 11) is present in vacuum and to some extent at 50% H coverage.

coverage as thermodynamic variables.[29] The present approach allows us, however, to treat the H pressure (instead of the H coverage) as the externally controlled thermodynamic variable. This accounts for the fact that a surface in contact with a gas reservoir can be considered as a combination of a closed system (the metal sublattice) and an open system (the hydrogen-vacancy sublattice), which in the present work is handled by sampling the two sublattices in canonical and SGC ensembles, respectively. This also allows us to observe the ordering tendencies that are apparent from the plateaus in the layer-by-layer concentration profiles (Figure 11) but do not reveal themselves from simpler thermodynamic models.

In the CuPd system, the variation of H coverage with H pressure is much more gradual than in the AuPd system (Figure 10). The transition occurs over a wide pressure interval similar to pure Pd, except for a shift to higher partial pressures (Figure 8b). At 0 and 100% H coverage, there is a pronounced depletion of Cu in the topmost layer. In contrast, at around 50% H coverage one observes a slight Cu enrichment that extends to a Cu bulk concentration of about 10% (Figure 12b). The Cu concentration in the second layer continuously decreases with H concentration, leading to a transition from strong Cu enrichment at 0% H coverage (Figure 12d) to a pronounced depletion at 100% H coverage (Figure 12f). This results in oscillatory concentration profiles between the layers at 0% (Figure 12a,d,g) and to some extent at 50% H coverage (Figure 12b,e,h), but not at 100% H coverage (Figure 12c,f,i). The rather intricate coupling in the case of CuPd between H coverage and the composition of both layers 1 and 2 is remarkable and highlights the complexity that can arise even in rather simple but concentrated multicomponent systems.

Our results for the H-rich limit are in accordance with previous experimental[65] and theoretical[29] work. As noted earlier,[25] there appears, however, to be a discrepancy between primarily experimental and theoretical studies (including the present) of CuPd in vacuum. Several experimental studies report Pd enrichment in the surface region (approximately six atomic layers) and Cu enrichment in the topmost surface layer(s).[33−35] Computational studies, however, report a slight Pd enrichment in the topmost surface layer,[26] at least for low Cu concentrations.[29,32] It has been suggested that this discrepancy is due to the oscillatory segregation energy profile,[25] which, as we have shown here, leads to concentration

https://doi.org/10.1021/acs.jpcc.1c00575
J. Phys. Chem. C 2021, 125, 17248−17260

oscillations between layers 1 and 2. The interplay between H coverage and surface composition described above provides an alternative explanation. Previous computational studies considered the segregation behavior either at 0 or 100% coverage for which the segregation energy of Cu in the topmost layer of a Pd{111} surface is positive, leading to Cu depletion (Figure 4c). As noted above, on the Pd-rich side the Cu concentration in the topmost layer is, however, largest at 50% H coverage (Figure 10), leading to Cu enrichment in both layers 1 and 2 up to a Cu bulk concentration of about 10% (Figure 12b,e). Furthermore, as a result of the gradual variation of H coverage with H pressure (Figure 8b), 0% H coverage should only be attainable at extremely small pressures ($\lesssim 1 \times 10^{-10}$ bar; Figure 8b), while at typical synthesis or operating conditions the H coverage most likely falls in the intermediate region closer to 50% (Figure 10b–d). The experimentally observed Cu enrichment could thus be the result of the nontrivial surface composition dependence on H coverage. We still note that other factors can be involved, including uncertainties in our models, experimental conditions, surface defects, and orientation.

The sensitivity of H coverage to both temperature and H pressure as well as its coupling to the Cu composition in the first two surface layers revealed here demonstrates that great care must be taken when interpreting experiments and calculations and extrapolating from ambient to operating conditions. In this regard, the role of the surface orientation deserves further investigation as adsorption and segregation have been previously observed to be sensitive to surface orientation.[29] It should also be insightful to apply the present approach to ternary surfaces such as AuCuPd, which could exhibit an even more intricate behavior.

CONCLUSIONS

In this study, we have analyzed the surface composition and segregation at AuPd and CuPd{111} surfaces as a function of H pressure, temperature, and bulk composition. To this end, we constructed CEs based on DFT calculations that we subsequently sampled by MC simulations. To deal with the large number of parameters in the CEs, we exploited local symmetries and physical intuition to merge orbits and thereby reduced the number of ECIs substantially. The resulting CEs provide reliable and accurate representations of the relevant energy landscape and can also be more efficiently sampled thanks to the lower number of ECIs.

Using this approach, we have found that the topmost layer of AuPd{111} surfaces switches from Au to Pd excess going from H-poor to H-rich conditions. This transition is very sharp as a function of H pressure, while it is weakly dependent on Au bulk concentration up to about 40% before rising sharply. The CuPd{111} surface exhibits a rather different behavior, exhibiting a more gradual variation of the H coverage with H pressure and Cu content. Remarkably, the Cu concentration in the topmost surface layer varies nonmonotonically with H coverage, exhibiting a maximum around 50% coverage. The latter even translates into a surface Cu enrichment up to a bulk Cu concentration of about 10%, providing a possible rationale for a previously noted discrepancy between calculations and experiments for this system.

Both systems, but in particular, the case of CuPd, demonstrate the rich behavior that can result from the interplay of metal–metal and metal–hydrogen interactions at surfaces, even in apparently simple systems. The results thereby also demonstrate the advantages of the concerted approach employed here that combines atomistic MC simulations based on lattice Hamiltonians trained against first-principles calculations with thermodynamic analysis.

ASSOCIATED CONTENT

Supporting Information

The Supporting Information is available free of charge at https://pubs.acs.org/doi/10.1021/acs.jpcc.1c00575.

Convergence of the DFT calculations; H adsorption energies; comparison of mixing energies from DFT and CE; CE comparison in Pd limit; ECIs of the final CEs; H chemical potential vs H coverage and near-surface composition for all layers; model construction and error quantification; composition of the training data sets; parameters used for CE training; and thermodynamics of H adsorption (PDF)

AUTHOR INFORMATION

Corresponding Author

Paul Erhart − *Department of Physics, Chalmers University of Technology, S-412 96 Gothenburg, Sweden;* orcid.org/0000-0002-2516-6061; Email: erhart@chalmers.se

Author

Pernilla Ekborg-Tanner − *Department of Physics, Chalmers University of Technology, S-412 96 Gothenburg, Sweden;* orcid.org/0000-0002-9427-4816

Complete contact information is available at: https://pubs.acs.org/10.1021/acs.jpcc.1c00575

Author Contributions

Databases with the results of DFT calculations, CEs, and averaged data from MC simulations along with pertinent scripts are provided via zenodo at https://doi.org/10.5281/zenodo.5076169.

Notes

The authors declare no competing financial interest.

ACKNOWLEDGMENTS

Funding from the Swedish Research Council (2015-04153 and 2018-06482), the Swedish Foundation for Strategic Research (RMA15-0052), and the Excellence Initiative Nano at Chalmers is gratefully acknowledged. The computations were enabled by resources provided by the Swedish National Infrastructure for Computing (SNIC) at NSC, C3SE, and PDC, partially funded by the Swedish Research Council through grant agreement no. 2018-05973.

REFERENCES

(1) Dutta, S. A review on production, storage of hydrogen and its utilization as an energy resource. *J. Ind. Eng. Chem.* **2014**, *20*, 1148–1156.

(2) Kast, J.; Vijayagopal, R.; Gangloff, J. J.; Marcinkoski, J. Clean commercial transportation: Medium and heavy duty fuel cell electric trucks. *Int. J. Hydrogen Energy* **2017**, *42*, 4508–4517.

(3) Kendall, K.; Kendall, M.; Liang, B.; Liu, Z. Hydrogen vehicles in China: Replacing the Western Model. *Int. J. Hydrogen Energy* **2017**, *42*, 30179–30185.

(4) Zenith, F.; Isaac, R.; Hoffrichter, A.; Thomassen, M. S.; Møller-Holst, S. Techno-economic analysis of freight railway electrification by overhead line, hydrogen and batteries: Case studies in Norway and USA. *Proc. Inst. Mech. Eng., Part F* **2020**, *234*, 791–802.

(5) Holladay, J. D.; Hu, J.; King, D. L.; Wang, Y. An overview of hydrogen production technologies. *Catal. Today* **2009**, *139*, 244−260.
(6) Abe, J. O.; Popoola, A. P. I.; Ajenifuja, E.; Popoola, O. M. Hydrogen energy, economy and storage: Review and recommendation. *Int. J. Hydrogen Energy* **2019**, *44*, 15072−15086.
(7) Najjar, Y. S. H. Hydrogen safety: The road toward green technology. *Int. J. Hydrogen Energy* **2013**, *38*, 10716−10728.
(8) Langhammer, C.; Zorić, I.; Kasemo, B.; Clemens, B. M. Hydrogen Storage in Pd Nanodisks Characterized with a Novel Nanoplasmonic Sensing Scheme. *Nano Lett.* **2007**, *7*, 3122−3127.
(9) Langhammer, C.; Larsson, E. M.; Kasemo, B.; Zorić, I. Indirect Nanoplasmonic Sensing: Ultrasensitive Experimental Platform for Nanomaterials Science and Optical Nanocalorimetry. *Nano Lett.* **2010**, *10*, 3529−3538.
(10) Bévenot, X.; Trouillet, A.; Veillas, C.; Gagnaire, H.; Clément, M. Surface plasmon resonance hydrogen sensor using an optical fibre. *Meas. Sci. Technol.* **2002**, *13*, 118−124.
(11) Tobiška, P.; Hugon, O.; Trouillet, A.; Gagnaire, H. An integrated optic hydrogen sensor based on SPR on palladium. *Sens. Actuators, B* **2001**, *74*, 168−172.
(12) Darmadi, I.; Nugroho, F. A. A.; Langhammer, C. High-Performance Nanostructured Palladium-Based Hydrogen Sensors-Current Limitations and Strategies for Their Mitigation. *ACS Sens.* **2020**, *5*, 3306−3327.
(13) Wadell, C.; Nugroho, F. A. A.; Lidström, E.; Iandolo, B.; Wagner, J. B.; Langhammer, C. Hysteresis-Free Nanoplasmonic Pd-Au Alloy Hydrogen Sensors. *Nano Lett.* **2015**, *15*, 3563−3570.
(14) Nugroho, F. A. A.; Darmadi, I.; Zhdanov, V. P.; Langhammer, C. Universal Scaling and Design Rules of Hydrogen-Induced Optical Properties in Pd and Pd-Alloy Nanoparticles. *ACS Nano* **2018**, *12*, 9903−9912.
(15) Rahm, J. M.; Löfgren, J.; Fransson, E.; Erhart, P. A tale of two phase diagrams: Interplay of ordering and hydrogen uptake in Pd−Au−H. *Acta Mater.* **2021**, *211*, No. 116893.
(16) Ma, L.; Laasonen, K.; Akola, J. Catalytic Activity of AuCu Clusters on MgO(100): Effect of Alloy Composition for CO Oxidation. *J. Phys. Chem. C* **2017**, *121*, 10876−10886.
(17) Sansa, M.; Dhouib, A.; Guesmi, H. Density functional theory study of CO-induced segregation in gold-based alloys. *J. Chem. Phys.* **2014**, *141*, No. 064709.
(18) Padama, A. A. B.; Villaos, R. A. B.; Albia, J. R.; Diño, W. A.; Nakanishi, H.; Kasai, H. CO-induced Pd segregation and the effect of subsurface Pd on CO adsorption on CuPd surfaces. *J. Phys.: Condens. Matter* **2016**, *29*, No. 025005.
(19) Darmadi, I.; Nugroho, F. A. A.; Kadkhodazadeh, S.; Wagner, J. B.; Langhammer, C. Rationally Designed PdAuCu Ternary Alloy Nanoparticles for Intrinsically Deactivation-Resistant Ultrafast Plasmonic Hydrogen Sensing. *ACS Sens.* **2019**, *4*, 1424−1432.
(20) Han, B. C.; Van der Ven, A.; Ceder, G.; Hwang, B.-J. Surface segregation and ordering of alloy surfaces in the presence of adsorbates. *Phys. Rev. B: Condens. Matter Mater. Phys.* **2005**, *72*, No. 205409.
(21) Kitchin, J. R.; Reuter, K.; Scheffler, M. Alloy surface segregation in reactive environments: First-principles atomistic thermodynamics study of Ag 3 Pd (111) in oxygen atmospheres. *Phys. Rev. B: Condens. Matter Mater. Phys.* **2008**, *77*, No. 075437.
(22) Løvvik, O. M.; Opalka, S. M. Reversed surface segregation in palladium-silver alloys due to hydrogen adsorption. *Surf. Sci.* **2008**, *602*, 2840−2844.
(23) Padama, A. A. B.; Kasai, H.; Budhi, Y. W. Hydrogen absorption and hydrogen-induced reverse segregation in palladium−silver surface. *Int. J. Hydrogen Energy* **2013**, *38*, 14715−14724.
(24) Atanasov, I.; Hou, M. Equilibrium ordering properties of Au-Pd alloys and nanoalloys. *Surf. Sci.* **2009**, *603*, 2639−2651.
(25) Løvvik, O. M. Surface segregation in palladium based alloys from density-functional calculations. *Surf. Sci.* **2005**, *583*, 100−106.
(26) Bozzolo, G.; Garcés, J. E.; Noebe, R. D.; Abel, P.; Mosca, H. O. Atomistic modeling of surface and bulk properties of Cu, Pd and the Cu-Pd system. *Prog. Surf. Sci.* **2003**, *73*, 79−116.
(27) Calvo, F. Thermodynamics of nanoalloys. *Phys. Chem. Chem. Phys.* **2015**, *17*, 27922−27939.
(28) Boes, J. R.; Kitchin, J. R. Modeling Segregation on AuPd(111) Surfaces with Density Functional Theory and Monte Carlo Simulations. *J. Phys. Chem. C* **2017**, *121*, 3479−3487.
(29) Zhao, M.; Sloof, W. G.; Bottger, A. Modelling of surface segregation for palladium alloys in vacuum and gas environments. *Int. J. Hydrogen Energy* **2018**, *43*, 2212.
(30) Mamatkulov, M.; Yudanov, I. V.; Bukhtiyarov, A. V.; Neyman, K. M. Pd Single-Atom Sites on the Surface of PdAu Nanoparticles: A DFT-Based Topological Search for Suitable Compositions. *Nanomaterials* **2021**, *11*, No. 122.
(31) Rousset, J. L.; Bertolini, J. C.; Miegge, P. Theory of segregation using the equivalent-medium approximation and bond-strength modifications at surfaces: Application to fcc Pd- X alloys. *Phys. Rev. B: Condens. Matter Mater. Phys.* **1996**, *53*, 4947−4957.
(32) Yang, L. Reverse surface segregation in Cu-Pd bimetallic catalysts at low concentrations of Cu. *Philos. Mag. A* **2000**, *80*, 1879−1888.
(33) Cheng, F.; He, X.; Chen, Z.-X.; Huang, Y.-G. Kinetic Monte Carlo simulation of surface segregation in Pd-Cu alloys. *J. Alloys Compd.* **2015**, *648*, 1090−1096.
(34) Miller, J. B.; Matranga, C.; Gellman, A. J. Surface segregation in a polycrystalline Pd70Cu30 alloy hydrogen purification membrane. *Surf. Sci.* **2008**, *602*, 375−382.
(35) Priyadarshini, D.; Kondratyuk, P.; Picard, Y. N.; Morreale, B. D.; Gellman, A. J.; Miller, J. B. High-Throughput Characterization of Surface Segregation in Cu_xPd_{1-x} Alloys. *J. Phys. Chem. C* **2011**, *115*, 10155−10163.
(36) Popov, A. A.; Shubin, Y. V.; Plyusnin, P. E.; Sharafutdinov, M. R.; Korenev, S. V. Experimental redetermination of the Cu−Pd phase diagram. *J. Alloys Compd.* **2019**, *777*, 204−212.
(37) Menning, C. A.; Chen, J. G. General trend for adsorbate-induced segregation of subsurface metal atoms in bimetallic surfaces. *J. Chem. Phys.* **2009**, *130*, No. 174709.
(38) Dhifallah, M.; Dhouib, A.; Aldulaijan, S.; Renzo, F. D. I.; Guesmi, H. First-principles study of Au−Cu alloy surface changes induced by gas adsorption of CO, NO, or O2. *J. Chem. Phys.* **2016**, *145*, No. 024701.
(39) Liu, M.; Yang, Y.; Kitchin, J. R. Semi-grand canonical Monte Carlo simulation of the acrolein induced surface segregation and aggregation of AgPd with machine learning surrogate models. *J. Chem. Phys.* **2021**, *154*, No. 134701.
(40) Chen, W.; Dalach, P.; Schneider, W. F.; Wolverton, C. Interplay between Subsurface Ordering, Surface Segregation, and Adsorption on Pt-Ti(111) Near-Surface Alloys. *Langmuir* **2012**, *28*, 4683−4693.
(41) Vignola, E.; Steinmann, S. N.; Le Mapihan, K.; Vandegehuchte, B. D.; Curulla, D.; Sautet, P. Acetylene Adsorption on Pd-Ag Alloys: Evidence for Limited Island Formation and Strong Reverse Segregation from Monte Carlo Simulations. *J. Phys. Chem. C* **2018**, *122*, 15456−15463.
(42) Müller, S.; Stöhr, M.; Wieckhorst, O. Structure and stability of binary alloy surfaces: Segregation, relaxation, and ordering from first-principles calculations. *Appl. Phys. A* **2006**, *82*, 415−419.
(43) Jian-Min, Z.; Fei, M.; Ke-Wei, X. Calculation of the surface energy of fcc metals with modified embedded-atom method. *Chin. Phys.* **2004**, *13*, 1082−1090.
(44) Løvvik, O. M.; Olsen, R. A. Adsorption energies and ordered structures of hydrogen on Pd(111) from density-functional periodic calculations. *Phys. Rev. B: Condens. Matter Mater. Phys.* **1998**, *58*, 10890−10898.
(45) Sanchez, J. M.; Ducastelle, F.; Gratias, D. Generalized cluster description of multicomponent systems. *Phys. A* **1984**, *128*, 334−350.
(46) van de Walle, A. Multicomponent multisublattice alloys, nonconfigurational entropy and other additions to the Alloy Theoretic Automated Toolkit. *Calphad* **2009**, *33*, 266−278.
(47) Ångqvist, M.; Muñoz, W. A.; Rahm, J. M.; Fransson, E.; Durniak, C.; Rozyczko, P.; Rod, T. H.; Erhart, P. ICET − A Python

Library for Constructing and Sampling Alloy Cluster Expansions. *Adv. Theory Simul.* **2019**, *2*, No. 1900015.
(48) Cao, L.; Li, C.; Mueller, T. The Use of Cluster Expansions To Predict the Structures and Properties of Surfaces and Nanostructured Materials. *J. Chem. Inf. Model.* **2018**, *58*, 2401−2413.
(49) Mueller, T.; Ceder, G. Bayesian approach to cluster expansions. *Phys. Rev. B: Condens. Matter Mater. Phys.* **2009**, *80*, No. 024103.
(50) Nelson, L. J.; Ozoliņš, V.; Reese, C. S.; Zhou, F.; Hart, G. L. W. Cluster expansion made easy with Bayesian compressive sensing. *Phys. Rev. B: Condens. Matter Mater. Phys.* **2013**, *88*, No. 155105.
(51) Blöchl, P. E. Projector augmented-wave method. *Phys. Rev. B: Condens. Matter Mater. Phys.* **1994**, *50*, 17953−17979.
(52) Kresse, G.; Joubert, D. From ultrasoft pseudopotentials to the projector augmented-wave method. *Phys. Rev. B: Condens. Matter Mater. Phys.* **1999**, *59*, 1758−1775.
(53) Kresse, G.; Hafner, J. Ab initio molecular dynamics for liquid metals. *Phys. Rev. B: Condens. Matter Mater. Phys.* **1993**, *47*, 558−561.
(54) Kresse, G.; Furthmüller, J. Efficiency of ab-initio total energy calculations for metals and semiconductors using a plane-wave basis set. *Comput. Mater. Sci.* **1996**, *6*, 15−50.
(55) Dion, M.; Rydberg, H.; Schröder, E.; Langreth, D. C.; Lundqvist, B. I. Van der Waals Density Functional for General Geometries. *Phys. Rev. Lett.* **2004**, *92*, No. 246401.
(56) Klimeš, J.; Bowler, D. R.; Michaelides, A. Van der Waals density functionals applied to solids. *Phys. Rev. B: Condens. Matter Mater. Phys.* **2011**, *83*, No. 195131.
(57) Berland, K.; Hyldgaard, P. Exchange functional that tests the robustness of the plasmon description of the van der Waals density functional. *Phys. Rev. B: Condens. Matter Mater. Phys.* **2014**, *89*, No. 035412.
(58) Gharaee, L.; Erhart, P.; Hyldgaard, P. Finite-temperature properties of nonmagnetic transition metals: Comparison of the performance of constraint-based semilocal and nonlocal functionals. *Phys. Rev. B: Condens. Matter Mater. Phys.* **2017**, *95*, No. 085147.
(59) Pathria, R. K.; Beale, P. D. *Statistical Mechanics*; Elsevier Ltd., 1996.
(60) Sadigh, B.; Erhart, P. Calculation of excess free energies of precipitates via direct thermodynamic integration across phase boundaries. *Phys. Rev. B: Condens. Matter Mater. Phys.* **2012**, *86*, No. 134204.
(61) Mitsui, T.; Rose, M. K.; Fomin, E.; Ogletree, D. F.; Salmeron, M. Hydrogen adsorption and diffusion on Pd(111). *Surf. Sci.* **2003**, *540*, 5−11.
(62) Johansson, M.; Skúlason, E.; Nielsen, G.; Murphy, S.; Nielsen, R. M.; Chorkendorff, I. Hydrogen adsorption on palladium and palladium hydride at 1bar. *Surf. Sci.* **2010**, *604*, 718−729.
(63) Engel, T.; Kuipers, H. A molecular-beam investigation of the scattering, adsorption and absorption of H2 and D2 from/on/in Pd(111). *Surf. Sci.* **1979**, *90*, 162−180.
(64) Rahm, J. M.; Tiburski, C.; Rossi, T. P.; Nugroho, F. A. A.; Nilsson, S.; Langhammer, C.; Erhart, P. A Library of Late Transition Metal Alloy Dielectric Functions for Nanophotonic Applications. *Adv. Funct. Mater.* **2020**, *30*, No. 2002122.
(65) Zhang, X.; Wang, W.; Liu, J.; Sheng, S.; Xiong, G.; Yang, W. Hydrogen transport through thin palladium-copper alloy composite membranes at low temperatures. *Thin Solid Films* **2008**, *516*, 1849−1856.

https://doi.org/10.1021/acs.jpcc.1c00575
J. Phys. Chem. C 2021, 125, 17248−17260

Supporting Information

Hydrogen-driven Surface Segregation in Pd-alloys from Atomic Scale Simulations

Pernilla Ekborg-Tanner and Paul Erhart
Chalmers University of Technology, Department of Physics, S-412 96 Gothenburg, Sweden

Contents

Tables

Table S1: Training data sets. Detailed description of training data sets divided into groups based on alloy and H coverage (Vac: 0%, H: 100% and HVac: 1-99% H coverage).

Data set	Number of structures	layers	Method
AuPd:Vac			
Pure Au, Pd	2	10	
Random	148	10	Random atomic configurations with randomly selected cell dimensions (up to 3×3 atoms per layer) and concentration selected from 10%, 20%, ..., 90% with triangular distribution*.
Segregation energy	10	10	Start with slab with 2×2 atoms per layer of species A, systematically replace one atom in layer 1, 2, ..., 5 with species B (for segregation energy calculation)**.
Orthogonal	197	12	Find structures that produces an orthogonal cluster space with cutoffs $2.5a_0$ (pairs) and $1.25a_0$ (triplets) without merged orbits, as described in Sect. Training data generation of the main paper***.
Adsorption energy	5	10	Build a CE (with training data sets listed above) and produce 5 low energy configurations with 25 % Au by simulated annealing of a cell with 3×3 atoms per layer (for adsorption energy calculation)****.
AuPd:H			
Pure AuH, PdH	2	10	
Orthogonal	58	10	*** with cutoffs $1.5a_0$ (pairs) and $0.75a_0$ (triplets).
Simulated annealing	49	10	Build a CE (with training data sets listed above) and produce new configurations by simulated annealing with randomly selected cell dimensions (up to 3×3 atoms per layer) and randomly selected concentration from triangular distribution*****.
Segregation energy	10	10	**
AuPd:HVac			
Orthogonal	87	10	*** with cutoffs $2.0a_0$ (pairs) and $1.25a_0$ (triplets).
Adsorption energy	83	10	All adsorption sites on the structures from ****.
CuPd:Vac			
Pure Pd	1	10	
Random	82	10	*
Segregation energy	5	10	**
Orthogonal	89	12	***
CuPd:H			
Pure CuH, PdH	1	10	
Orthogonal	36	10	*** with cutoffs $1.5a_0$ (pairs) and $0.75a_0$ (triplets).
Simulated annealing	20	10	*****
Segregation energy	5	10	**
CuPd:HVac			
Orthogonal	44	10	*** with cutoffs $2.0a_0$ (pairs) and $1.25a_0$ (triplets).

Notes

Supplementary Note 1: Parameters for CE training

The `icet` package (1) was used for CE construction. We used cutoffs $2.0a_0$ (pairs) and $1.25a_0$ (triplets) and merging of orbits (as described in Sect. Introducing local symmetries of the main paper) such that training data with 10- and 12-layers could be utilized. The cutoffs was selected from a large set of cutoffs up to Training consists of a solving a linear problem $Ax = b$ and automatic relevance detection regression (ARDR) was used to that end.

The threshold lambda parameter, which controls the sparsity of the solution vector, was selected based on Bayesian information criterion (BIC) minimization using the following procedure. Training was performed for a range of lambda threshold values and a fit of the BIC value as a function lambda threshold was executed using cubic interpolation. The resulting fitted curve was minimized with respect to BIC, and the corresponding lambda threshold was selected for the final model (9246 for AuPd:H and 3144 for CuPd:H).

The numerical tolerance for determining convergence of the solution vector x is set to 10^{-6}. CV-RMSE was calculated using a 10-fold split (with shuffling). The fit matrix and target values were standardized before fitting, meaning that all columns were rescaled to have a standard deviation of 1.0.

Supplementary Note 2: Thermodynamics of H adsorption

To determine if H adsorption is favorable at a certain H_2 partial pressure p and temperature T, we need to study the difference in Gibbs free energy

$$\Delta G(T, p) = E_{\text{ads}} - \mu_{\text{H}}(T, p). \tag{1}$$

where E_{ads} is the adsorption energy and $\mu_{\text{H}}(T, p)$ is the chemical potential of gas-phase H. The adsorption energy can be calculated from DFT calculations

$$E_{\text{ads}} = E^{\text{DFT}}_{\text{slab:H}} - E^{\text{DFT}}_{\text{slab}} - \frac{1}{2}E^{\text{DFT}}_{\text{H}_2}$$

and the chemical potential is given by (assuming ideal gas behavior)

$$\mu_{\text{H}}(T, p) = \frac{1}{2}\left(\mu^{\circ}_{\text{H}_2}(T) + k_B T \ln \frac{p_{\text{H}_2}}{p^{\circ}_{\text{H}_2}}\right)$$

where $p^{\circ}_{\text{H}_2}$ and $\mu^{\circ}_{\text{H}_2}(T)$ are the reference pressure and chemical potential from Eq. 4.

Adsorption is favorable when $\Delta G(T, p) < 0$. We can thus calculate the minimum pressure $p^*(T, E_{\text{ads}})$ required for adsorption at a site with a certain adsorption energy by rewriting Eq. (1) and setting $\Delta G(T, p) = 0$

$$p^*(T, E_{\text{ads}}) = p^{\circ} \exp \frac{2E_{\text{ads}} - \mu^{\circ}_{\text{H}_2}(T)}{kT}.$$

.

Figures

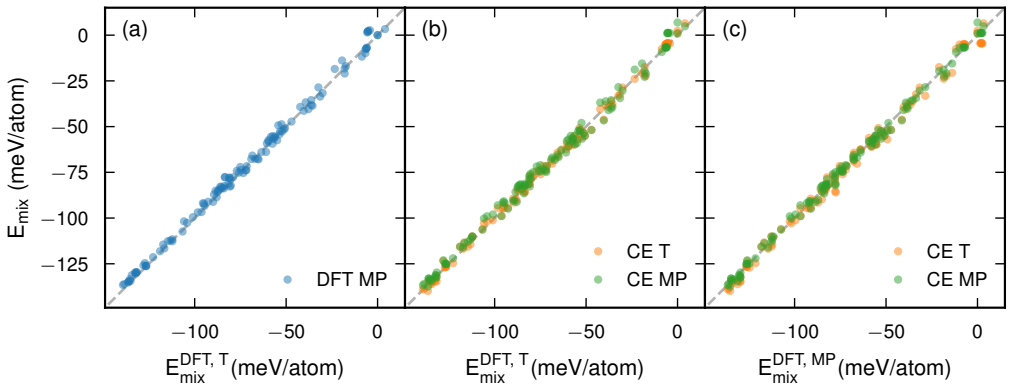

Figure S1: Impact of $\boldsymbol{k}$-point density and smearing method. CEs for the AuPd:H system are trained using the final energy calculations (tetrahedron method with Blöchl corrections and $\boldsymbol{k}$-point density 0.1 Å^{-1}) and the last step of the atomic relaxation (Methfessel-Paxon method and $\boldsymbol{k}$-point density 0.2 Å^{-1}). Note that these models are from a previous iteration of this project where H was not explicitly included in the CE and cutoffs 1.5 and 0.75 Åwere used for pairs and triplets, respectively. The correlation between density-functional theory (DFT) calculations using the tetrahedron method (T) and Methfessel-Paxon method with fewer $\boldsymbol{k}$-points (MP) is presented in (a). In (b-c), the corresponding correlations between DFT and CE energies is presented, with respect to the tetrahedron (b) or Methfessel-Paxon (c) DFT energies. The difference between the two approaches is small.

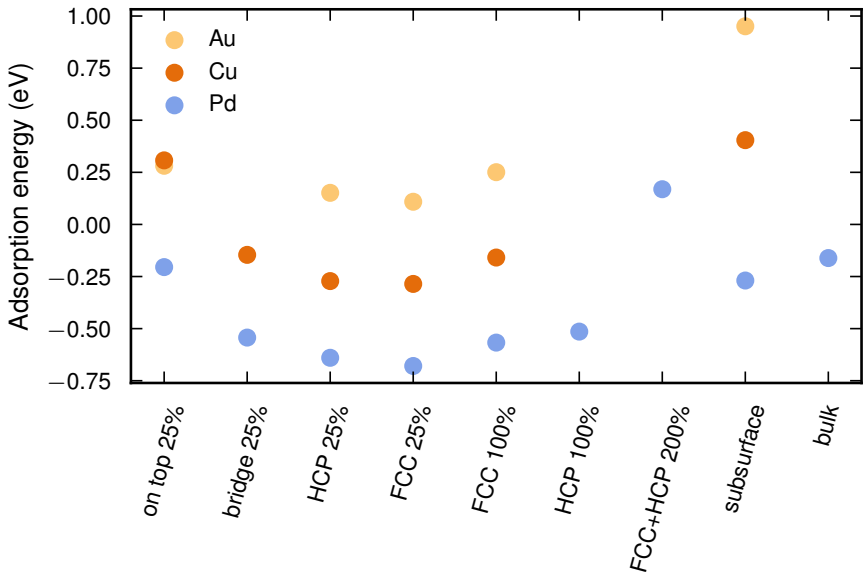

Figure S2: H adsorption energy on Pd, Au and Cu. H adsorption energy at different sites and coverages over pure Pd, Au and Cu. The coverage is defined in terms of number of adsorbates per surface metal atom. For all metals, 25% coverage at the face-centered cubic (FCC) site is lowest in energy. The hexagonal close-packed (HCP) site is very close in energy, but full coverage at FCC and HCP sites (200% coverage) is very unfavorable and H would go to the subsurface and bulk before that scenario. As a result, it is sufficient to consider FCC sites only.

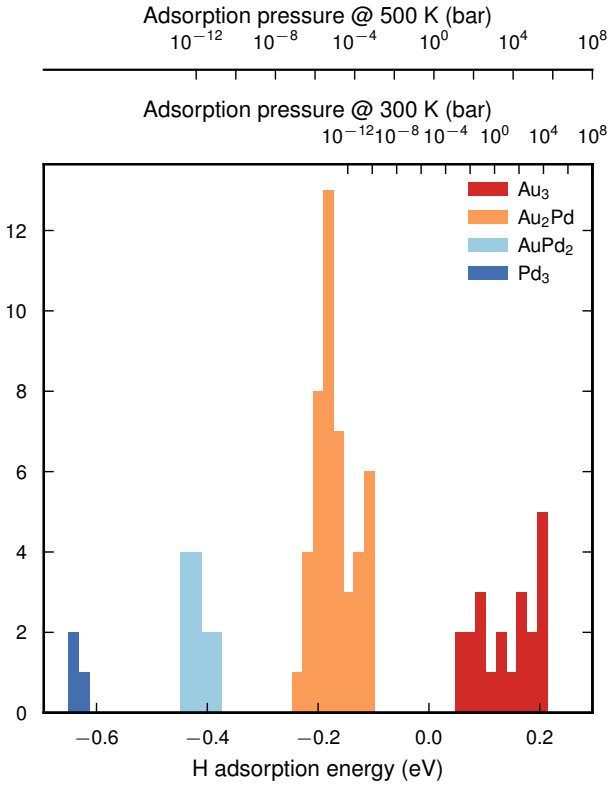

Figure S3: Hydrogen adsorption energy on PdAu. Adsorption energies for all FCC H-sites of five atomic configurations consisting of 75% Pd and 25% Au. The configurations are $3 \times 3 \times 10$-atom surface slabs obtained from simulated annealing at 300 K in vacuum. The adsorption energies are clustered info four groups, which are determined by the configuration of metal atoms below the H-site, as indicated. The upper x-axes show the corresponding minimum pressure required for adsorption, calculated as outlined in Supplementary Note 2. At ambient conditions, adsorption is favorable on sites above at least one Pd atom.

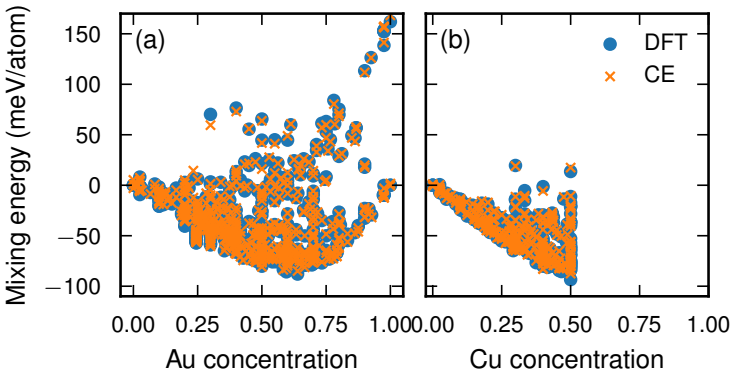

Figure S4: Comparison of DFT and CE mixing energy. Mixing energies of all structures in the training set for (a) AuPd:H and (b) CuPd:H.

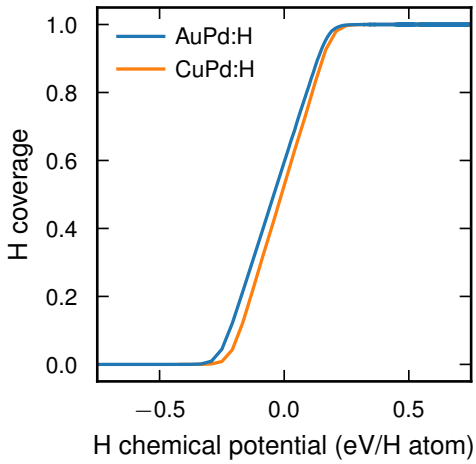

Figure S5: Pd limit for AuPd:H and CuPd:H CEs. H coverage as a function of H chemical potential for pure Pd based on Monte Carlo (MC) simulations of the AuPd:H and CuPd:H CEs. The models are in good agreement.

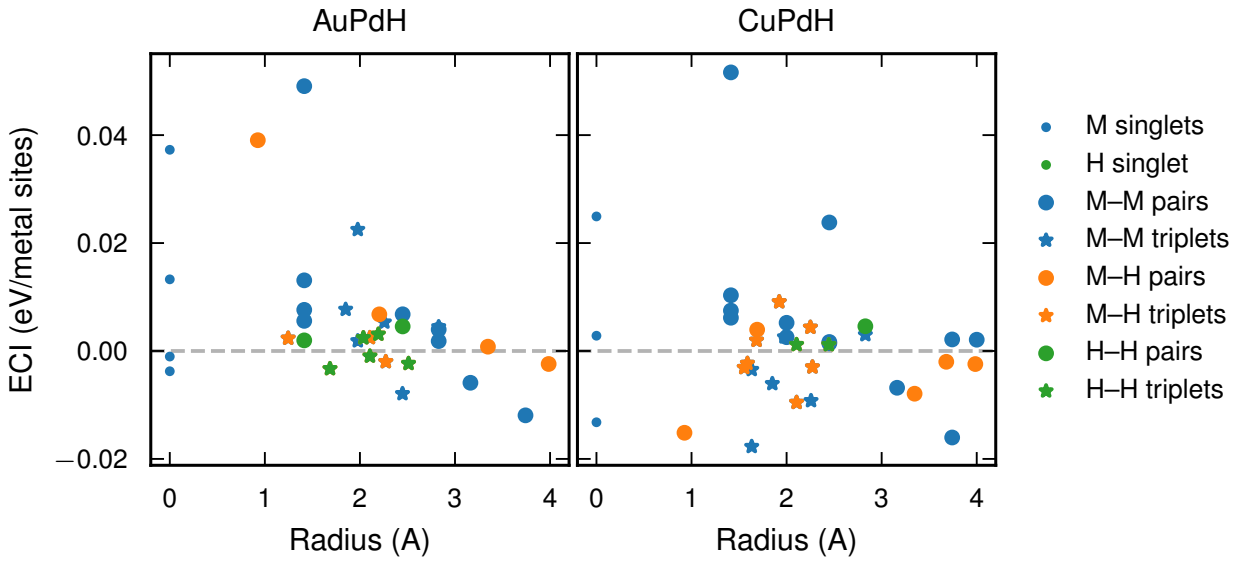

Figure S6: Fitted ECIs for the final CEs. The mixing energy is to a large extent determined by the singlets as well as small radius clusters and the effective cluster interactions (ECIs) decay quickly with radius.

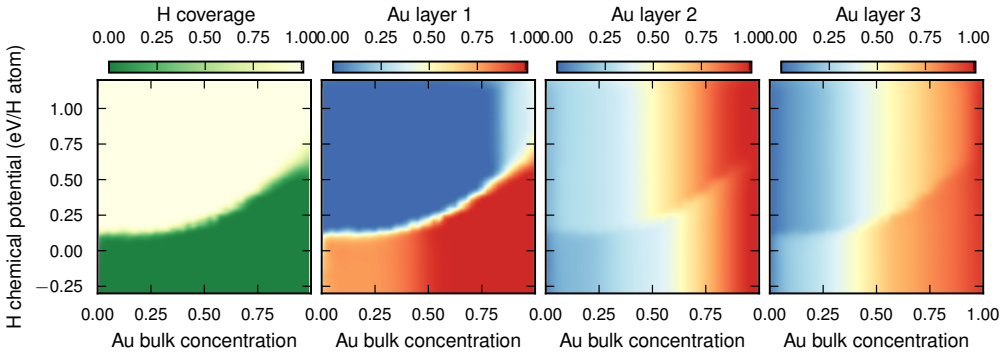

Figure S7: Chemical potential vs. surface state for AuPd:H. Chemical potential vs. coverage and near-surface composition for AuPd:H at 300 K for the near-surface region.

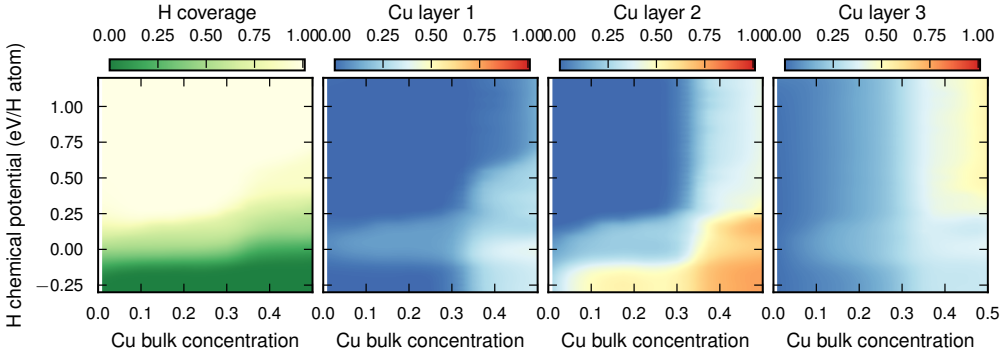

Figure S8: Chemical potential vs. surface state for CuPd:H. Chemical potential vs. coverage and near-surface composition for CuPd:H at 300 K for the near-surface region.

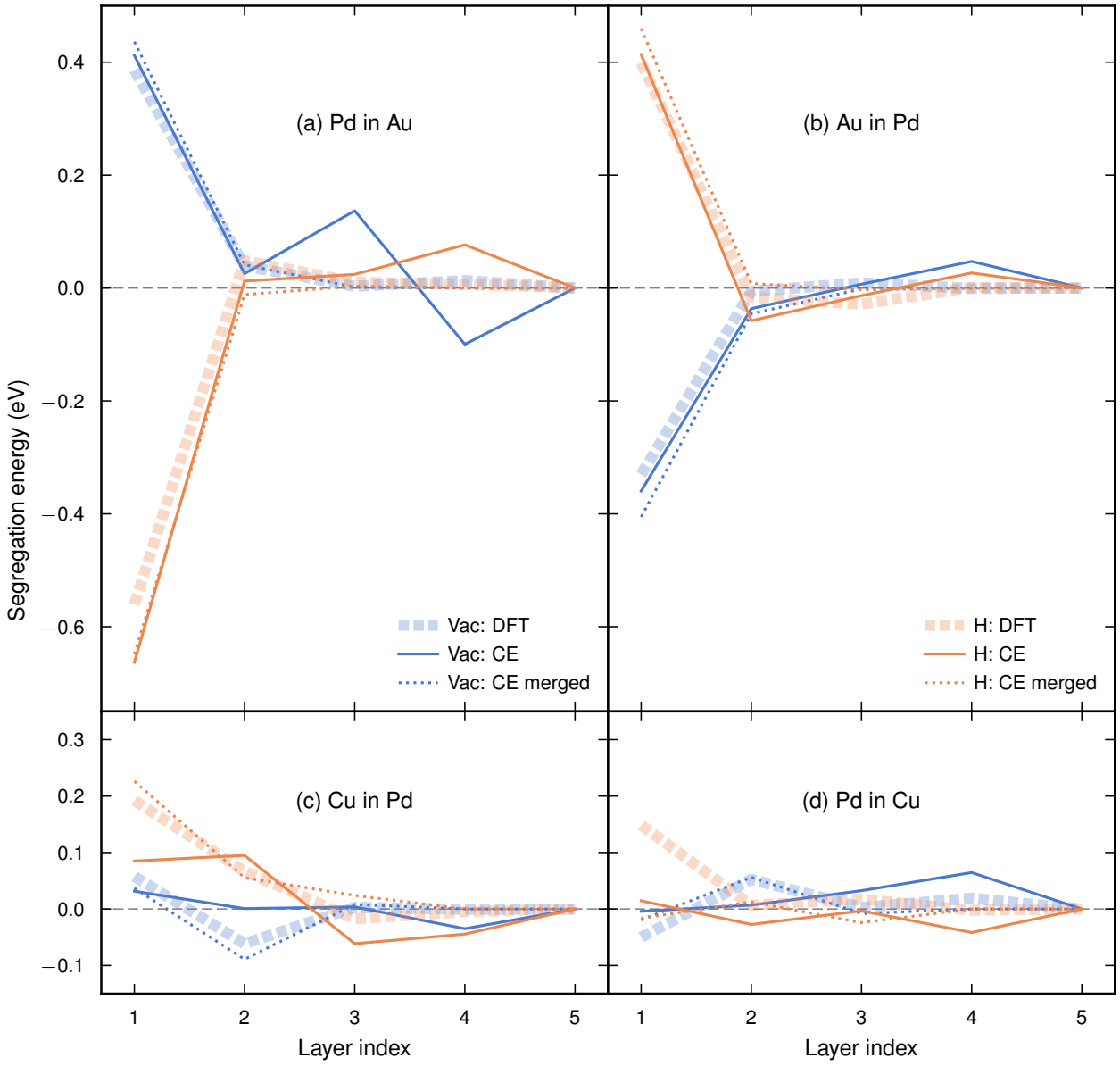

Figure S9: Effect of merged orbits on segregation energy. CEs were trained with and without merging orbits using training sets consisting of all 10-layer structures with 0% or 100% coverage. Note that these models are from a previous iteration of this project where H was not explicitly included in the CE and cutoffs 1.5 and 0.75 Åwere used for pairs and triplets, respectively. The segregation energy prediction of CEs without merged orbits (solid) differs significantly more from the DFT results (dashed) compared to the CEs with merged orbits. Note that for these models, the CV-RMSE was lower without merged orbits, suggesting overfitting.

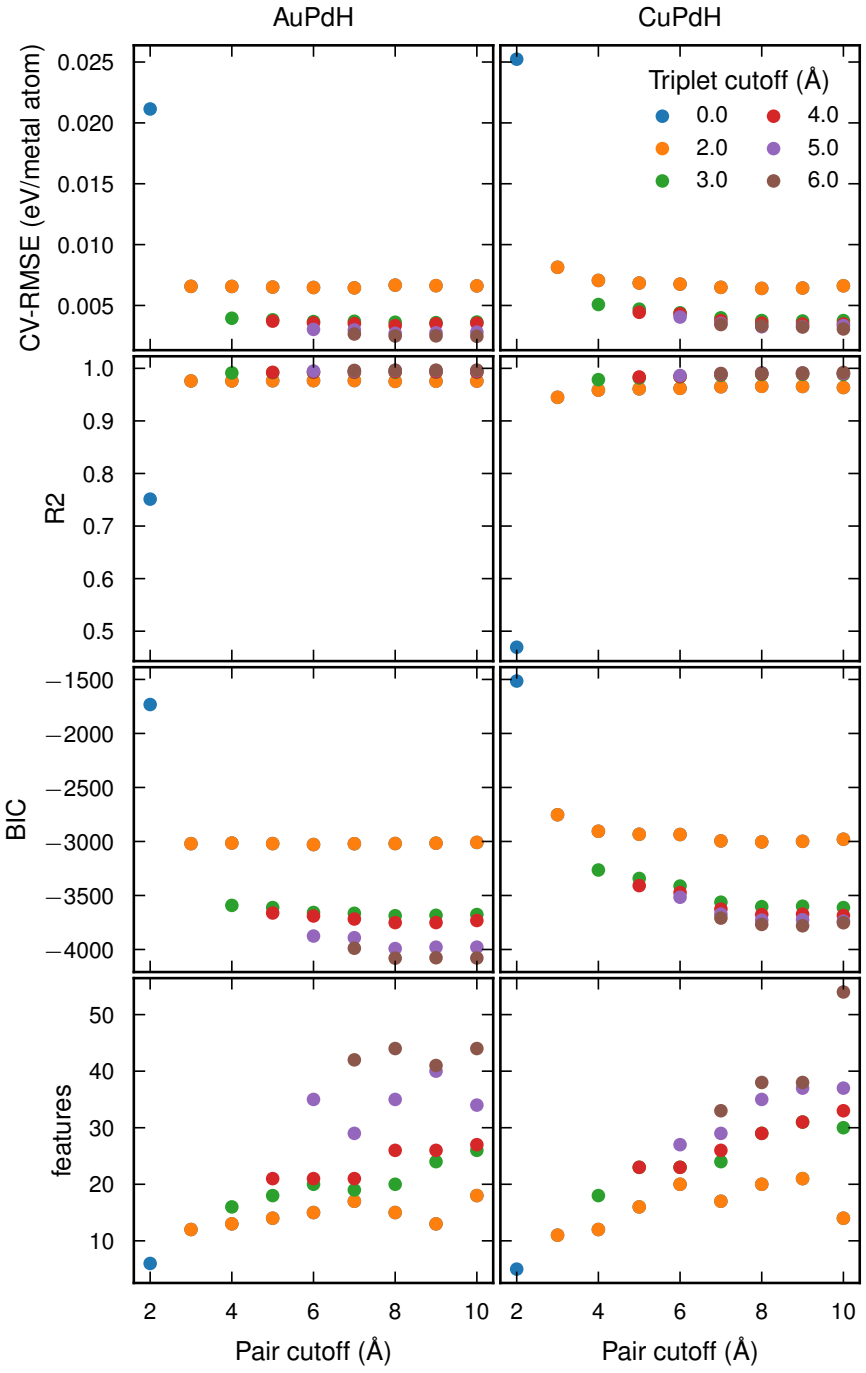

Figure S10: Effect of cutoffs during training. Performance of CEs trained as outlined in the main text using different cutoffs (the first and second value correspond to the pair and triplet cutoff, respectively). According to these metrics, higher cutoffs yield better models due to the larger number of features but there is also a risk of overfitting. We selected cutoffs 8.0 Å for pairs and 5.0 Å for triplets, where the BIC score in particular seems to have converged.

Supplementary References

[1] M. Ångqvist, W. A. Muñoz, J. M. Rahm, E. Fransson, C. Durniak, P. Rozyczko, T. H. Rod, and P. Erhart, *ICET – A Python Library for Constructing and Sampling Alloy Cluster Expansions,* Advanced Theory and Simulations **2**, 1900015 (2019). doi:10.1002/adts.201900015.